



# The Molecular Gas in the NGC 6240 Merging Galaxy System at the Highest Spatial Resolution

Ezequiel Treister<sup>1</sup> , Hugo Messias<sup>2</sup> , George C. Privon<sup>3</sup> , Neil Nagar<sup>4</sup> , Anne M. Medling<sup>5</sup> , Vivian U<sup>6</sup> , Franz E. Bauer<sup>7,8,9</sup> , Claudia Cicone<sup>10,11</sup> , Loreto Barcos Muñoz<sup>2,12,13</sup> , Aaron S. Evans<sup>12,13</sup> , Francisco Muller-Sanchez<sup>14</sup> , Julia M. Comerford<sup>15</sup> , Lee Armus<sup>16</sup> , Chin-Shin Chang<sup>2</sup> , Michael Koss<sup>17</sup> , Giacomo Venturi<sup>1</sup> , Kevin Schawinski<sup>18,19</sup> , Caitlin Casey<sup>20</sup> , C. Megan Urry<sup>21</sup> , David B. Sanders<sup>22</sup> , Nicholas Scoville<sup>23</sup> , and Kartik Sheth<sup>24</sup> 

<sup>1</sup> Instituto de Astrofísica, Facultad de Física, Pontificia Universidad Católica de Chile, Casilla 306, Santiago 22, Chile; [etreiste@astro.puc.cl](mailto:etreiste@astro.puc.cl)

<sup>2</sup> Joint ALMA Observatory, Alonso de Córdova 3107, Vitacura, Santiago, Chile

<sup>3</sup> Department of Astronomy, University of Florida, 211 Bryant Space Science Center, Gainesville, FL 32611, USA

<sup>4</sup> Universidad de Concepción, Departamento de Astronomía, Casilla 160-C, Concepción, Chile

<sup>5</sup> Ritter Astrophysical Research Center, University of Toledo, Toledo, OH 43606, USA

<sup>6</sup> Department of Physics and Astronomy, 4129 Frederick Reines Hall, University of California, Irvine, CA 92697, USA

<sup>7</sup> Instituto de Astrofísica and Centro de Astroingeniería, Facultad de Física, Pontificia Universidad Católica de Chile, Casilla 306, Santiago 22, Chile

<sup>8</sup> Millennium Institute of Astrophysics (MAS), Nuncio Monseñor Sótero Sanz 100, Providencia, Santiago, Chile

<sup>9</sup> Space Science Institute, 4750 Walnut Street, Suite 205, Boulder, CO 80301, USA

<sup>10</sup> INAF—Osservatorio Astronomico di Brera, Via Brera 28, I-20121 Milano, Italy

<sup>11</sup> Institute of Theoretical Astrophysics, University of Oslo, Postboks 1029, NO-0315 Oslo, Norway

<sup>12</sup> Department of Astronomy, University of Virginia, 530 McCormick Road, Charlottesville, VA 22904, USA

<sup>13</sup> National Radio Astronomy Observatory, 520 Edgemont Road, Charlottesville, VA 22903, USA

<sup>14</sup> Physics Department, University of Memphis, Memphis, TN 38152, USA

<sup>15</sup> Department of Astrophysical and Planetary Sciences, University of Colorado, Boulder, CO 80309, USA

<sup>16</sup> Spitzer Science Center, California Institute of Technology, Pasadena, CA 91125, USA

<sup>17</sup> Eureka Scientific, 2452 Delmer Street, Suite 100, Oakland, CA 94602-3017, USA

<sup>18</sup> Institute for Particle Physics and Astrophysics, ETH Zurich, Wolfgang-Pauli-Str. 27, CH-8093 Zurich, Switzerland

<sup>19</sup> Modulos AG, Technoparkstrasse 1, CH-8005 Zurich, Switzerland

<sup>20</sup> Department of Astronomy, The University of Texas at Austin, 2515 Speedway Boulevard Stop C1400, Austin, TX 78712, USA

<sup>21</sup> Yale Center for Astronomy & Astrophysics, Physics Department, New Haven, CT 06520, USA

<sup>22</sup> Institute for Astronomy, 2680 Woodlawn Drive, University of Hawaii, Honolulu, HI 96822, USA

<sup>23</sup> Cahill Center for Astrophysics, California Institute of Technology, 1216 East California Boulevard, Pasadena, CA 91125, USA

<sup>24</sup> NASA Headquarters, 300 E Street SW, Washington, DC 20546, USA

Received 2019 September 4; revised 2019 December 26; accepted 2020 January 2; published 2020 February 24

## Abstract

We present the highest-resolution—15 pc ( $0''.03$ )—ALMA  $^{12}\text{CO}(2-1)$  line emission and 1.3 mm continuum maps, tracers of the molecular gas and dust, respectively, in the nearby merging galaxy system NGC 6240, which hosts two supermassive black holes growing simultaneously. These observations provide an excellent spatial match to existing *Hubble Space Telescope* (*HST*) optical and near-infrared observations of this system. A significant molecular gas mass,  $\sim 9 \times 10^9 M_{\odot}$ , is located between the two nuclei, forming a clumpy stream kinematically dominated by turbulence, rather than a smooth rotating disk, as previously assumed from lower-resolution data. Evidence for rotation is seen in the gas surrounding the southern nucleus but not in the northern one. Dynamical shells can be seen, likely associated with nuclear supernova remnants. We further detect the presence of significant high-velocity outflows, some of them reaching velocities  $> 500 \text{ km s}^{-1}$ , affecting a significant fraction,  $\sim 11\%$ , of the molecular gas in the nuclear region. Inside the spheres of influence of the northern and southern supermassive black holes, we find molecular masses of  $7.4 \times 10^8$  and  $3.3 \times 10^9 M_{\odot}$ , respectively. We are thus directly imaging the reservoir of gas that can accrete onto each supermassive black hole. These new ALMA maps highlight the critical need for high-resolution observations of molecular gas in order to understand the feeding of supermassive black holes and its connection to galaxy evolution in the context of a major galaxy merger.

*Unified Astronomy Thesaurus concepts:* Galaxy mergers (608); Galaxy interactions (600); Active galaxies (17); AGN host galaxies (2017); Active galactic nuclei (16); Molecular gas (1073)

*Supporting material:* animation

## 1. Introduction

In our current understanding of galaxy evolution, major galaxy–galaxy mergers play a fundamental role (Sanders et al. 1988; Hopkins et al. 2008) in both the cosmic history of star formation and the growth of their central supermassive black

holes (SMBHs). Computational simulations (e.g., Barnes & Hernquist 1991) show that the dynamical interactions between merging galaxies cause gas to lose angular momentum and fall into the center of each nucleus, triggering significant episodes of both star formation and SMBH accretion and generating a so-called luminous active galactic nucleus (AGN; Treister et al. 2012; Glikman et al. 2015; Kocevski et al. 2015; Fan et al. 2016; Trakhtenbrot et al. 2017; Weston et al. 2017; Donley et al. 2018; Goulding et al. 2018; Weigel et al. 2018). In this scenario, the relatively short-lived phase,  $\sim 1\text{--}100$  Myr, in

which both SMBHs are growing simultaneously (dual AGNs) is the critical period when black hole and star formation activity is the most vigorous (Van Wassenhove et al. 2012; Blecha et al. 2013, 2018).

The prototypical dual AGN is often considered to be NGC 6240. Based on existing optical images, NGC 6240 was classified as a late-stage compact merger (e.g., de Vaucouleurs et al. 1964). *Chandra*X-ray observations carried out by Komossa et al. (2003) and later by Wang et al. (2014) revealed two nuclei in hard X-rays, 2–8 keV, separated by  $\sim 2''$  ( $\sim 950$  pc), each with prominent Fe K $\alpha$  emission, a clear indicator of AGN activity (e.g., Nandra & Pounds 1994). The masses of each SMBH have been estimated dynamically with resolved integral field spectroscopy at  $\sim 9 \times 10^8 M_\odot$  (Medling et al. 2015). While the observed  $E < 10$  keV X-ray luminosities for each nucleus are relatively modest,  $L_X \sim 10^{42}$  erg s $^{-1}$ , the *Swift*/BAT observations at  $E = 14$ –195 keV (Baumgartner et al. 2013) show that their intrinsic, absorption-corrected luminosities (and hence SMBH accretion rates) are significantly higher. A very high IR luminosity of  $0.9 \times 10^{12} L_\odot$  (Veilleux et al. 2009) also places NGC 6240 right at the lower limit for the ultraluminous IR galaxy (ULIRG) classification. Additionally, earlier observations of the molecular gas in this merging system indicate that most of the gas can be found between the two nuclei (Bryant & Scoville 1999, and many others since), not around them. Hence, most of the IR emission appears to be attributed to star formation processes rather than the AGN, likely arising from a significant starburst with an age  $< 20$  Myr, as revealed by near-IR (Tecza et al. 2000; Engel et al. 2010) and mid-IR spectroscopy (Inami et al. 2013; Stierwalt et al. 2013). Therefore, NGC 6240 is the ideal laboratory to study the interplay between AGNs and star formation in major galaxy mergers.

As argued by Tacconi et al. (1999) and Engel et al. (2010), NGC 6240 might represent an earlier evolutionary stage in which the gas is still in the process of settling in a central thin disk between the two nuclei. In the next stage, it will probably experience a major starburst event, such as those observed in Arp 220 and other ULIRGs (Downes & Solomon 1998). As discussed extensively in the past and clearly confirmed in this work, NGC 6240 is a very complex system. As such, it is not surprising that the determination of even basic physical parameters in this galaxy is still heavily debated in the literature. For example, the estimated global star formation rate ranges from a lower value of  $25 M_\odot \text{ yr}^{-1}$  (Engel et al. 2010) to  $> 100 M_\odot \text{ yr}^{-1}$  (Howell et al. 2010), while specific nuclear regions have been claimed to have values up to  $\sim 270 M_\odot \text{ yr}^{-1}$  (Pasquali et al. 2004).

Previous subarcsecond CO(2–1) observations of NGC 6240 using the IRAM Plateau de Bure interferometer carried out by Tacconi et al. (1999) indicated that most of the molecular gas was located between the two nuclei. Most of this gas was described as being in a turbulent, rotating, thick disk. This central gas concentration of  $\sim (2\text{--}4) \times 10^9 M_\odot$  represents  $\sim 30\%$ – $70\%$  of the dynamical mass of the system. This is, however, based on the assumed rotation in the central CO source. Similarly, later observations using the Submillimeter Array (SMA) by Iono et al. (2007) found that the  $^{12}\text{CO}(3\text{--}2)$  emission is extended on a  $4''$  scale (corresponding to  $\sim 1.9$  kpc), while in contrast, the HCO $^+$  (4–3) is strongly concentrated in the central kiloparsec between the two nuclei. Large velocity offsets of up to  $\sim 800$  km s $^{-1}$  were already

observed in the  $^{12}\text{CO}(1\text{--}0)$  emission of NGC 6240, thanks to IRAM observations at  $\sim 1''$  resolution (Feruglio et al. 2013b). This provides a clear indication that AGN and/or supernova feedback is taking place in this system. Indeed, recently, Müller-Sánchez et al. (2018) reported the presence of kiloparsec-scale ionized outflows in NGC 6240. Nonspatially overlapping ionized outflow rates of  $\sim 10$  and  $75 M_\odot \text{ yr}^{-1}$  were attributed to star formation and AGN feedback, respectively. Combined, they are comparable to the measured star formation rate in the system (Müller-Sánchez et al. 2018).

From neutral hydrogen (H I) observations, the recession velocity of the north and south nuclei are 7440 and 7258 km s $^{-1}$ , respectively (Beswick et al. 2001). Baan et al. (2007) posited that it is most plausible that the south nucleus lies behind the northern one, with the line joining the nuclei at  $13^\circ$  to the line of sight, i.e., a projection factor of 4.3. The projected separation between nuclei ( $\sim 1''.51$  at PA  $\sim 19^\circ$ ) would thus correspond to a true distance of  $\sim 3.2$  kpc. The stellar velocity field of the southern galaxy suggests a northwest–southeast rotation (PA =  $130^\circ$  to the receding side; inclination  $\sim 60^\circ$ ), and the northern galaxy suggests a southwest–northeast rotation (PA =  $61^\circ$  to the receding side; inclination  $i = 33''\text{--}52''$ ; Baan et al. 2007; Medling et al. 2011, 2014). It is argued that shells and bubbles observed at radio wavelengths in this merger originate from outflows driven by the south nucleus (Heckman et al. 1990; Baan et al. 2007). Centimeter very long baseline interferometry (VLBI) observations of NGC 6240 (Hagiwara et al. 2011) have detected not only the two nuclei (previous nomenclature used: N1 for the south nucleus and N2 for the north nucleus) but also two radio supernovae: RS1, which is 35 mas southwest of the south nucleus, and RS2, which is  $0''.287$  northeast (PA  $28^\circ$ ) of the south nucleus.

Several Atacama Large Millimeter/submillimeter Array (ALMA) observations have targeted NGC 6240. Scoville et al. (2015) used dust continuum observations at 350 (Band 7) and 696 (Band 9) GHz to derive a nuclear interstellar medium (ISM) mass of  $1.6 \times 10^9 M_\odot$  in an  $\sim 200$  pc radius. More recently, Saito et al. (2018) presented ALMA CO(2–1) Band 6 observations of this system at moderate resolutions,  $\sim 1 \times 0.5$  arcsec $^2$ , finding—in addition to the central concentration—extended high-velocity ( $\sim 2000$  km s $^{-1}$ ) components with a total mass of  $5 \times 10^8 M_\odot$ . Similarly, four broad components located  $\sim 1$ – $2$  kpc away from the center of the system were reported. Finally, Cicone et al. (2018) combined [C I](1–0) and CO(2–1) ALMA observations with IRAM Plateau de Bure Interferometer CO(1–0) maps to trace molecular outflows in the central  $6 \times 3$  kpc $^2$  region of NGC 6240. They found outflowing molecular gas peaking between the two SMBHs and extending by several kpc along the east–west direction. The total H $_2$  outflow rate is  $2500 \pm 1200 M_\odot \text{ yr}^{-1}$ , where the error includes the uncertainty on the  $\alpha_{\text{CO}}$  factor, hence confirming that a combination of AGN and star formation feedback is required to drive the observed outflows. Similar to the values of the star formation rate, the mass outflow rate in different parts of the system is very relevant for this work and can vary by more than an order of magnitude, ranging from  $\sim 230$  (Saito et al. 2018) up to  $\sim 2500 M_\odot \text{ yr}^{-1}$  in the central region (Cicone et al. 2018), due to different assumptions for the geometry of the outflow and the position where the outflow is measured. The range in these measurements will be considered in our analysis and interpretation of this system.

**Table 1**  
The Characteristics of Each EB Considered in This Study

Date [UTC]	EB [uid://A002/...]	Base <sub>min</sub> <sup>max</sup> (m)	res/MRS (arcsec)	$N_{\text{ANT}}$	Flux	Bandpass	Phase	Check	ToS (min)
2015 Nov 1 17:24–18:38 UT	Xac5575/X8a5f	14969 84.7	0.024 0.38	41	J1550 +0527	J1550+0527	J1651 +0129	J1649 +0412	32
2016 Jan 29 10:46–11:02 UT	Xaf985b/Xf3f	331 15.1	0.97 9.3	44	J1550 +0527	J1550+0527	J1651 +0129	J1659 +0213	1.1
2016 May 31 04:09–04:33 UT	Xb3c4ab/Xbef	784 15.1	0.44 5.12	39	J1550 +0527	J1751+0939	J1651 +0129	J1659 +0213	2.1
2016 Jul 28 04:17–04:41 UT	Xb5fdce/X79d	1124 15.1	0.26 3.51	42	Pallas	J1751+0939	J1651 +0129	J1659 +0213	2.1
2017 Sep 29 23:39–00:49 UT	Xc5148b/ X127e	14969 41.4	0.023 0.46	43	J1751 +0939	J1751+0939	J1651 +0129	J1649 +0412	35
2016 Jun 26 13:29–13:53 UT	Xb4da9a/X69a	784 15.1	0.43 5.41	42	Titan	J1550+0527	J1651 +0129	...	4.2

**Note.** Date and time of observation; EB UID code; maximum and minimum baseline length; expected spatial resolution and maximum recoverable scale (res/MRS); number of antennas; sources used for flux, bandpass, and phase calibrator, together with the check source; and time on source (ToS), i.e., NGC 6240. Note that uid: [//A002/Xb4da9a/X69a](#) was observed as part of 2015.1.00003.S (Saito et al. 2018).

Here we present new ALMA observations of the  $^{12}\text{CO}(2-1)$  rotational transition with the highest angular resolution to date, using up to 15 km baselines. Section 2 presents the technical properties of the data and details of the data processing and reduction. Section 3 shows the results, including emission, kinematic, and velocity dispersion maps. These results are discussed in Section 4, while the conclusions are presented in Section 5. Throughout this paper, we assume a  $\Lambda\text{CDM}$  cosmology with  $h_0 = 0.7$ ,  $\Omega_m = 0.27$ , and  $\Omega_\Lambda = 0.73$  (Hinshaw et al. 2009).

## 2. ALMA Data

ALMA observed NGC 6240 as part of its Cycle 3 program 2015.1.00370.S (PI: E. Treister). The  $^{12}\text{CO}(2-1)$  at rest frame 230.538 GHz was targeted as a tracer of the molecular gas in the central region of the system. The achieved angular resolution is  $\sim 0''.03$ , corresponding to a physical scale of  $\sim 15$  pc,  $\sim 10\times$  higher than previous observations of this and similar molecular transitions (Tacconi et al. 1999; Iono et al. 2007; Wilson et al. 2008; Scoville et al. 2015; Cicone et al. 2018; Saito et al. 2018). Furthermore, this is comparable and slightly better than existing *Hubble Space Telescope* (*HST*) optical imaging (Geressen et al. 2004) and  $>2\times$  sharper than near-IR *HST* maps (Scoville et al. 2000). Previous ground-based observations assisted by adaptive optics, presented by Max et al. (2007), reached similar spatial resolutions at near-IR wavelengths. The main technical goal of our program was to obtain the highest possible resolution maps of the  $^{12}\text{CO}(2-1)$  emission, while at the same time recovering most of the total flux at large scales by combining three different array configurations (baselines from 15 m to 15 km). The observations were divided on two science goals, comprised of three different configuration groups overall. Data from program 2015.1.00003.S (Saito et al. 2018) were also included to improve the recovery of the large-scale structure from intermediate-length baselines.

### 2.1. Description of Observations

Table 1 details the properties of each observation considered in this study. Despite not being used in the final imaging for the reasons listed below, the long baseline execution block (EB) Xac5575/X8a5f is also listed. All of the observations described, except Xb4da9a/X69a, share the same spectral setup. The total ALMA bandwidth of 7.5 GHz was divided into four spectral windows (SPWs) of 1875 MHz each and a spectral resolution of 1.953 MHz. In all observations, one of these SPWs was specifically tuned to study the redshifted  $^{12}\text{CO}(2-1)$  transition, centered at a frequency of 225.1 GHz. The remaining ones were used to trace the millimeter continuum centered at frequencies of 227.5, 239.9, and 241.9 GHz, with the second one partly covering the CS(5–4) line. The Xb4da9a/X69a EB covered the  $^{12}\text{CO}(2-1)$  and CS(5–4) transitions with two SPWs centered at 224.9 and 239.8 GHz with spectral resolutions of 1.953 and 3.906 MHz, respectively. The remaining two SPWs traced the continuum at 221.9 and 237.9 GHz with spectral resolutions of 7.813 MHz.

### 2.2. Data Analysis

For the data analysis, the Common Astronomy Software Applications (CASA, v5.4; McMullin et al. 2007) was used. In general, the standard ALMA data reduction<sup>25</sup> approach was pursued, with some specific differences. More details about the array configuration properties, observations, processing method, and imaging parameters are reported in the Appendix.

## 3. Results

### 3.1. NGC 6240 $^{12}\text{CO}(2-1)$ Emission

Figure 1 shows the  $^{12}\text{CO}(2-1)$  emission, together with the optical imaging provided by the *HST* using the Wide Field Planetary Camera 2 (WFPC2) instrument. As described above, by combining low- and high-resolution observations, we are

<sup>25</sup> Available at <https://almascience.nrao.edu/processing/science-pipeline>.

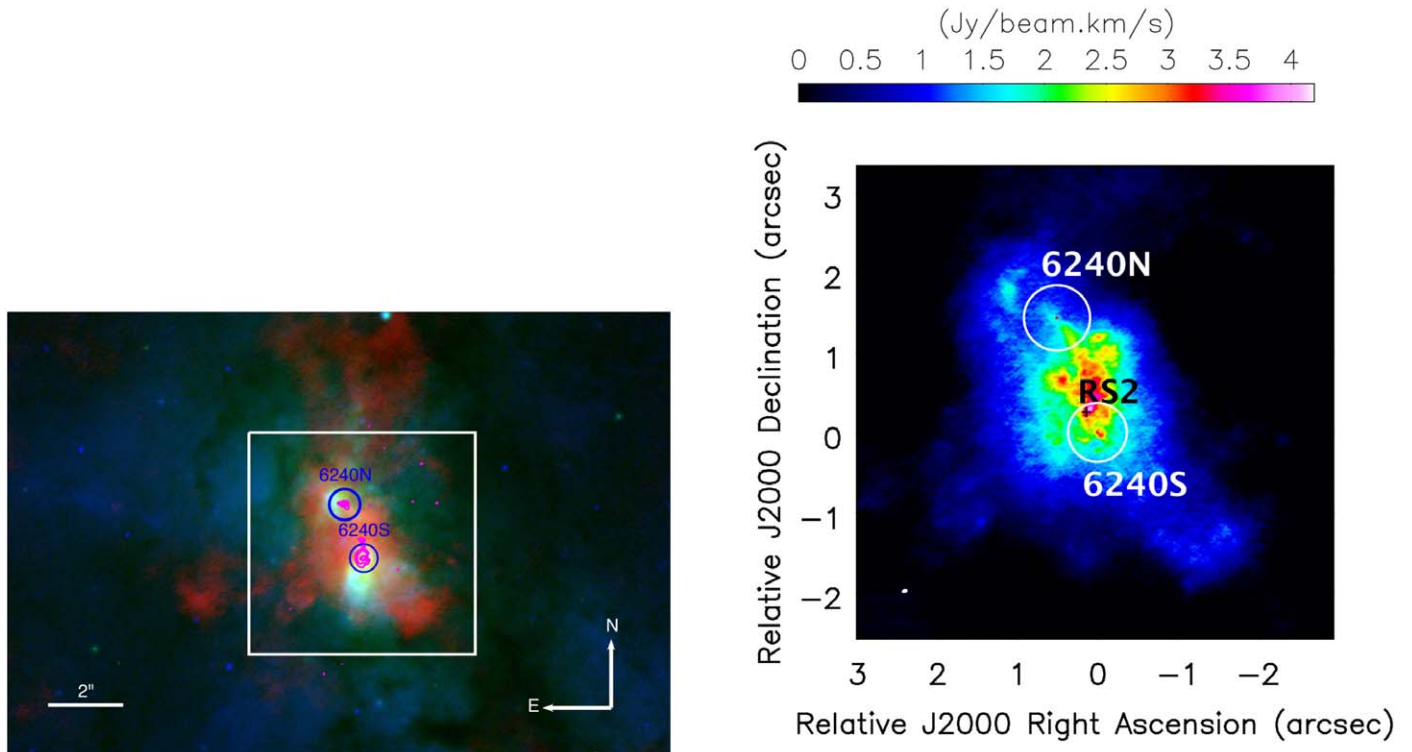


**Figure 1.** Left panel: central region of the NGC 6240 system covering approximately  $13 \times 8 \text{ kpc}^2$  ( $2'' \simeq 1 \text{ kpc}$ ). Blue and green denote images from the *HST*/WFPC2 in the F450W and F814W bands, respectively. Red denotes the moment 0 ALMA  $^{12}\text{CO}(2-1)$  observations presented here. The blue circles mark the locations of the north and south nuclei based on VLBI radio observations (Hagiwara et al. 2011). Magenta contours show the continuum emission at 235 GHz, as obtained from our ALMA data and presented in Figure 2, in five logarithmic levels starting from  $4 \times 10^{-5} \text{ Jy beam}^{-1}$  and ending at  $4 \times 10^{-3} \text{ Jy beam}^{-1}$ . The white square presents the zoom region displayed in the right panel. There we show the integrated intensity map of the  $^{12}\text{CO}(2-1)$  emission, as observed by ALMA. White circles indicate the spheres of influence of each SMBH, as estimated by Medling et al. (2015) based on near-IR integral field spectroscopic observations obtained with the Keck telescopes, while their locations are shown by red dots. The black plus sign marks the position of the supernova RS2, as reported from radio observations by Hagiwara et al. (2011).

able to recover all of the emission out to scales of  $30''$ . Indeed, the total measured flux is  $1163 \pm 28 \text{ Jy km s}^{-1}$  in the ALMA field of view of  $25''$  diameter, which accounts for 95% of the total  $\text{CO}(2-1)$  when compared to the Tacconi et al. (1999) measurements. We can further compare this total flux to single-dish observations. An unresolved,  $^{12}\text{CO}(2-1)$  flux of  $1492 \pm 253 \text{ Jy km s}^{-1}$  was reported by Greve et al. (2009), implying that our ALMA observations recover 67%–94% of the single-dish flux when considering the relatively large error bars of the Greve et al. (2009) measurements. As can be seen in Figure 1, a significant concentration of the molecular gas is found in the central regions, consistent with findings based on previous observations (e.g., Tacconi et al. 1999; Engel et al. 2010). However, extended molecular emission can be detected up to  $\sim 10''$  ( $\sim 5 \text{ kpc}$ ) away from the nuclear region. The bulk of the molecular gas emission in the nuclear region of the system appears to be directly connected to the material found between the nuclei.

This molecular CO emission does not spatially coincide with the submillimeter continuum observed by ALMA at observed frame 235 GHz, as shown by the magenta contours in the left panel of Figure 1 and in more detail in Figure 2. Similarly, the bulk of the  $^{12}\text{CO}(2-1)$  emission does not appear to overlap with the stellar light traced by the optical and near-IR emission either, which is mostly centered around each nucleus (Max et al. 2005; Engel et al. 2010). This could be naturally explained by the effects of dust extinction in the nuclear regions. Indeed, Max et al. (2005, 2007) and

Müller-Sánchez et al. (2018) reported the presence of significant dust lanes in the center of the NGC 6240 system. For our work, the nuclear positions were obtained from the VLBI observations of this source, as reported by Hagiwara et al. (2011). Specifically, the nuclear positions used are  $16^{\text{h}}52^{\text{m}}58.924$ ,  $02^{\circ}24'04''.776$  and  $16^{\text{h}}52^{\text{m}}58.890$ ,  $02^{\circ}24'03''.350$  for the northern and southern ones, respectively. The typical error in these positions is 0.6 mas. Only a relatively small fraction of the molecular gas, compared to the total amount in the central region of the system, is found inside the sphere of influence of each SMBH, which was computed by Medling et al. (2015) to have radii of  $235 \pm 8$  and  $212 \pm 9 \text{ pc}$  for the northern and southern nuclei, respectively, and are hence fully resolved in the ALMA cube. This can be used to improve existing measurements of the SMBH mass in each nucleus by separating the SMBH and molecular gas contributions to the total enclosed nuclear mass, which in turn indicates that these are closer to the usual  $M$ – $\sigma$  correlation than previously indicated (Medling et al. 2019). Recently, Kollatschny et al. (2020) claimed the detection of a third nucleus in this system from optical integral field spectroscopy observations close to the southern nucleus at a position of  $16^{\text{h}}52^{\text{m}}58.901$ ,  $02^{\circ}24'02''.88$ . We do not detect any significant  $^{12}\text{CO}(2-1)$  emission at this position or its surroundings, in stark contrast with the two previously established nuclei.

In contrast to previous submillimeter observations at lower spatial resolutions (Tacconi et al. 1999; Saito et al. 2018), the molecular gas in the nuclear region does not appear to follow a

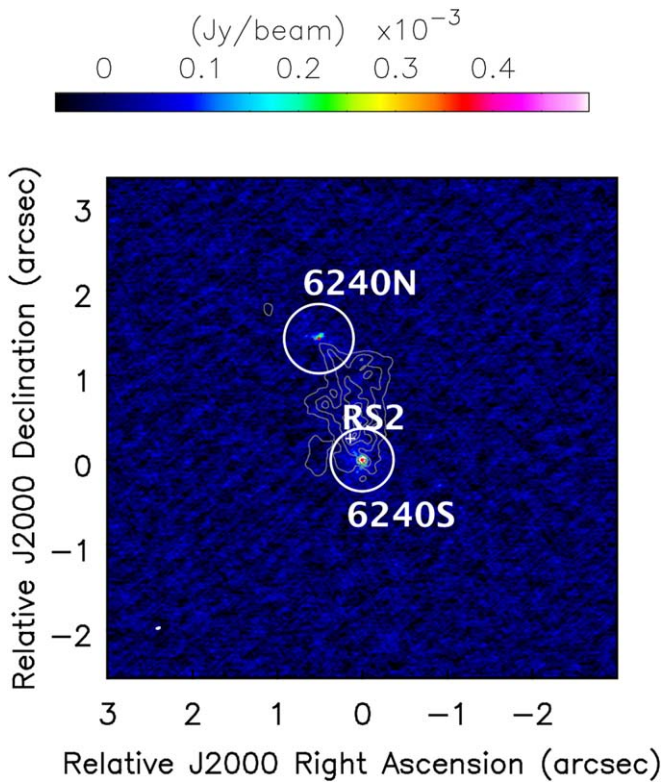


**Figure 2.** Millimeter continuum emission (color scale) in the central region of NGC 6240 at an effective observed-frame frequency of 235 GHz, as obtained from the ALMA observations described here. The white circles have radii of 235 and 212 pc for the north and south nuclei, respectively, corresponding to the spheres of influence of each SMBH, while the gray contours present the integrated (moment 0)  $^{12}\text{CO}(2-1)$  emission. The position of RS2 is indicated by the white plus sign. With an observed spectral index of  $-0.91$  (Hagiwara et al. 2011), the expected flux of RS2 ( $\sim 12 \mu\text{Jy}$ ) falls well below the sensitivity of these ALMA observations. Each contour shows an increase of 20% in flux starting from a base level of  $0.2 \text{ Jy beam}^{-1} \text{ km s}^{-1}$ . The beam size and shape of the continuum observations can be seen in white in the bottom left corner. As can be seen, the millimeter continuum emission is concentrated around each SMBH and shows little overlap with the molecular gas traced by the  $^{12}\text{CO}(2-1)$  transition.

smooth distribution. Instead, substantial clumpiness can be found on the stream that connects both nuclei, as can be seen in Figure 1. Similar structures in the spatial distribution of the molecular emission, in this case from  $^{12}\text{CO}(3-2)$  observations, have been previously presented by U et al. (2011) and Wang et al. (2014). These clumpy regions are natural sites where vigorous star formation should take place. However, according to high-resolution,  $\sim 0''.1$ , near-IR observations at  $2.2 \mu\text{m}$  obtained with the Very Large Telescope (VLT)/SINFONI integral field spectrograph, reported by Engel et al. (2010), the bulk of the nuclear stellar mass appears to precede the merger and is spatially concentrated around each nucleus, certainly much more than the molecular gas traced by the ALMA observations.

In order to take advantage of the superb spatial resolution of the ALMA observations, the focus of this work is mostly on the relatively small-scale, subarcsecond structures. That being said, we can place these in the context of more extended structures previously reported from CO observations. Specifically, Feruglio et al. (2013a) reported the detection of  $\text{CO}(1-0)$  emission extending up to  $20''$  ( $\sim 10 \text{ kpc}$ ) from the central region of the system in both the eastward and southwestward directions. The eastward extended structure is also detected

in our ALMA data at velocities of  $\sim -300$  to  $-400 \text{ km s}^{-1}$  and reaching up to  $\sim 12''$  at the edge of the field of view of our data cube; as such, we cannot verify a larger extension. We also detect the southwestward structure at a velocity of  $\sim -100 \text{ km s}^{-1}$ . The extension of this structure is  $\sim 13''$  from the southern nucleus, where it reaches the edge of the field of view, as in the previous case. Hence, we confirm the detection of extended CO emission previously reported by Feruglio et al. (2013a). We can further identify an additional extended structure reaching up to  $\sim 7''$  to the northwest of the northern nucleus at velocities of  $\sim 100-200 \text{ km s}^{-1}$ . A detailed characterization of these large-scale structures is beyond the scope of this paper.

### 3.2. Continuum Emission

As described in Section 2, some of the ALMA SPWs were used to study the continuum emission at  $\sim 235 \text{ GHz}$ , corresponding to  $\sim 1.25 \text{ mm}$ , which we show in Figure 2. As can be seen there, and contrary to what was observed for the  $^{12}\text{CO}(2-1)$  transition that mostly traces the molecular gas, the millimeter continuum emission arising from dust is mostly concentrated around each nucleus. We measure continuum flux densities at an observed-frame frequency of  $235 \text{ GHz}$  of  $9.92 \pm 0.16$  and  $3.50 \pm 0.037 \text{ mJy}$  inside the corresponding SMBH spheres of influence for the southern and northern nuclei, respectively. Considering now a much larger aperture with a diameter of  $22''$ , we measure a continuum flux of  $13.0 \pm 0.6 \text{ mJy}$ . Hence, we can conclude that in this source, most of the total millimeter continuum emission detected in our ALMA data is directly associated with the two nuclear regions. Furthermore, as can be seen in Figure 2, the emission is strongly concentrated and marginally resolved. Similar to the nondetection of  $\text{CO}(2-1)$  emission discussed in the previous section, at the flux limit of our observations, we do not detect any submillimeter continuum emission at the location of the third nucleus reported by Kollatschny et al. (2020).

The continuum fluxes reported here are significantly higher than those reported by Tacconi et al. (1999) at  $228 \text{ GHz}$ , by 2.1 times for the southern nucleus and 3.5 times for the northern one, using similar apertures  $\sim 0''.8$  in diameter. This discrepancy can likely be explained by sparse  $uv$  coverage by our long baseline observations combined with their poor phase stability, which particularly affects flux measurements on relatively small scales,  $\sim 1''$ , after integrating over a relatively large wavelength range. Indeed, when continuum fluxes are measured using only the compact and intermediate array configurations described in Appendix A.1, we obtain values of  $5.19 \pm 0.06$  and  $1.73 \pm 0.03 \text{ mJy}$  for the southern and northern nuclei, respectively, roughly consistent with the Tacconi et al. (1999) values. The discrepancy with the maps containing the long baselines is much smaller if we use much smaller apertures,  $< 0''.5$ , as was done by Medling et al. (2019), or much larger ones. Indeed, on a  $22''$  diameter aperture, we measure a continuum flux of  $10.1 \pm 0.13 \text{ mJy}$ , again showing that most of the millimeter continuum emission in this system is associated with the two nuclei. Therefore, in what follows, we only use these latter fluxes, as clearly better  $uv$  coverage and phase stability are required to measure continuum fluxes at relatively small scales. The continuum emission map presented in Figure 2 is, however, not significantly affected, as this “extra” flux has a relatively low surface density. Similarly, by comparing with previously reported  $^{12}\text{CO}(2-1)$  fluxes at a

range of scales and resolutions, we concluded that our line measurements have not been significantly affected. Hence, this issue is only relevant for continuum studies that require one to integrate flux densities over a large wavelength range. Note that the use of feathering on a per-channel basis when retrieving the  $^{12}\text{CO}(2-1)$  emission map prevented this low surface density from being parsed to the final combined map.

Previously, Nakanishi et al. (2005) presented continuum observations at frequencies of 87 and 108 GHz, with synthesized beam sizes of  $\sim 2''$  and  $\sim 4''$  and total measured fluxes of 16.6 and 10.8 mJy at each frequency, respectively. Even at lower spatial resolution, both Tacconi et al. (1999) and Nakanishi et al. (2005) were able to identify an offset between the continuum and the line emission, which is further corroborated by our ALMA data. The spectral shape in these data is given by a power law with index  $\alpha = -0.81$ , consistent with synchrotron emission from nonthermal sources such as AGNs or supernova remnants. Our ALMA observations reveal that most of the continuum emission arises from the surroundings of each SMBH and is significantly brighter than the extrapolation of the spectrum at low frequencies, as presented in Section 4.2, thus strongly suggesting that this radiation is dominated by dust heated by AGN activity.

The existing 880  $\mu\text{m}$  single-dish dust continuum measurement of NGC 6240 is  $F_{880} = 133 \pm 40$  mJy (Wilson et al. 2008). Adopting a dust emissivity index  $\beta = 1.8$  (Planck Collaboration et al. 2011), this predicts a flux density at 235 GHz of  $32 \pm 10$  mJy. Hence, our observations recover approximately 41% of the expected continuum flux. If we assume this missing flux is concentrated in a central  $2''$  diameter aperture, the predicted flux per beam is 5  $\mu\text{Jy}$ , below our detection threshold. The missing flux is hence consistent with being due to insufficient surface brightness sensitivity in these continuum observations.

### 3.3. Gas Kinematics

The ALMA observations also yield information about the kinematics of the molecular gas. Figure 3 shows the velocity map for the central region of NGC 6240 as traced by the  $^{12}\text{CO}(2-1)$  emission. In contrast to previous claims (Bryant & Scoville 1999; Tacconi et al. 1999; Engel et al. 2010), there is no clear evidence for a rotating disk in the internuclear region. In fact, no well-defined structures are obviously visible in the moment 1 map. A similar conclusion, albeit using lower-resolution data, was reached before by Ciccone et al. (2018). In this work, they reported that the typical butterfly pattern, a smoking gun for a rotating disk, could not be seen; it is not present in our data either. Instead, they concluded that the kinematics in the nuclear region were dominated by outflows. The higher-resolution ALMA data appear consistent with a significant high-velocity outflow, described in more detail in Section 4.3, visible directly south of the northern nucleus. A tentative velocity gradient can also be observed between the two nuclei. Indeed, such a velocity gradient, of  $\sim 100$   $\text{km s}^{-1}$ , was previously reported based on subarcsecond  $^{12}\text{CO}(3-2)$  observations by Iono et al. (2007) and U et al. (2011). This gradient was also found in the  $\text{H}_2$  observations of this region reported by Müller-Sánchez et al. (2018), who interpreted it as a perturbed turbulent rotational disk. To facilitate the visualization of the overall kinematical structure of the cold molecular gas in the nuclear region of NGC 6240, Figure 4 presents a snapshot of an animation available in the electronic

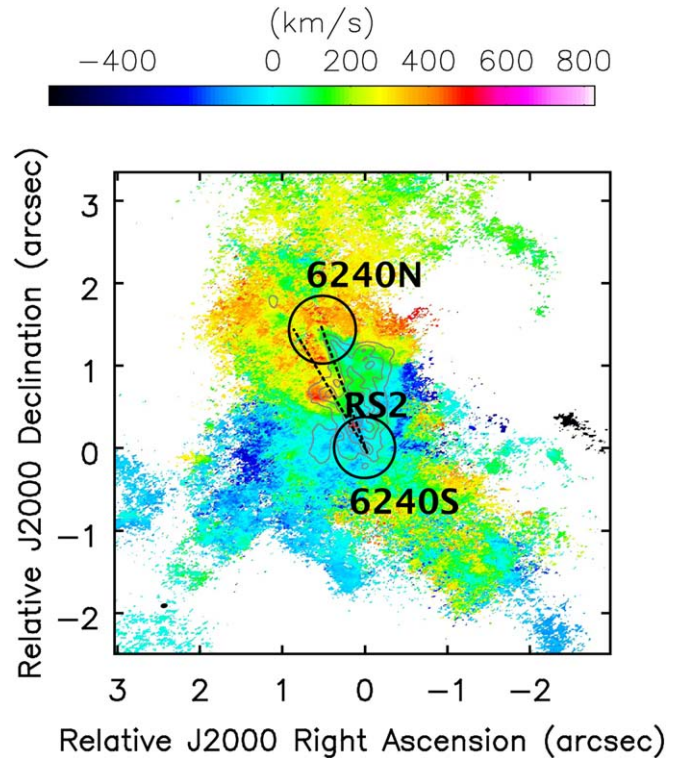


**Figure 3.** Velocity (moment 1) map for the  $^{12}\text{CO}(2-1)$  emission from the ALMA data presented here. Black circles show  $\sim 200$  pc diameter circles, corresponding to the spheres of influence for each SMBH, as described in Figure 1. The red plus sign marks the position of RS2, while the two dashed lines show the locations connecting the two nuclei and between the southern nucleus and RS2 where  $p$ - $v$  diagrams were extracted, as shown in Figures 5 and 7, respectively. A hint of a velocity gradient, ranging from  $\sim 300$   $\text{km s}^{-1}$  in the northern region to  $\sim -150$   $\text{km s}^{-1}$ , can be seen in the stream connecting both nuclei. In addition, we can see high-velocity regions at  $>500$   $\text{km s}^{-1}$ , as those described in Figure 10, corresponding to a molecular gas outflow.

version of this paper exploring the three-dimensional spatial and velocity cube traced by our ALMA observations.

In order to better understand the kinematic structure of the molecular gas stream connecting the two nuclei, Figure 5 presents a position-velocity ( $p$ - $v$ ) diagram along a slit connecting the two nuclei. For illustration, we overplot the velocity field predictions of the respective stellar disk only and stellar disk plus black hole in the northern and southern nuclei using parameters from Medling et al. (2011, 2015) and assuming, for simplicity, that the PA and inclination of the inner gas disks around the north and south SMBHs follow the same kinematics as the larger-scale stellar disk.<sup>26</sup> First, near the southern nucleus, located inside the sphere of influence of the southern SMBH, we can see a strongly localized gradient over  $\sim 0''.2$  spanning a range of approximately  $\pm 200$   $\text{km s}^{-1}$ . The CO velocities here do not follow the rotating stellar disk model posited by Medling et al. (2015). This gas thus either follows a different orientation or projection or traces outflowing nuclear gas (in which case, the near side of the southern stellar disk (S) is to the northeast). Interpreting the northeast side of the southern galaxy as the near side would be consistent with the model of Baan et al. (2007), in which the southern stellar disk is behind the northern one (N). Extrapolating this further,

<sup>26</sup> This need not be the case but is assumed for simplicity, since there is insufficient information to determine the kinematics of the gas from the  $\text{CO}(2-1)$  emission alone.

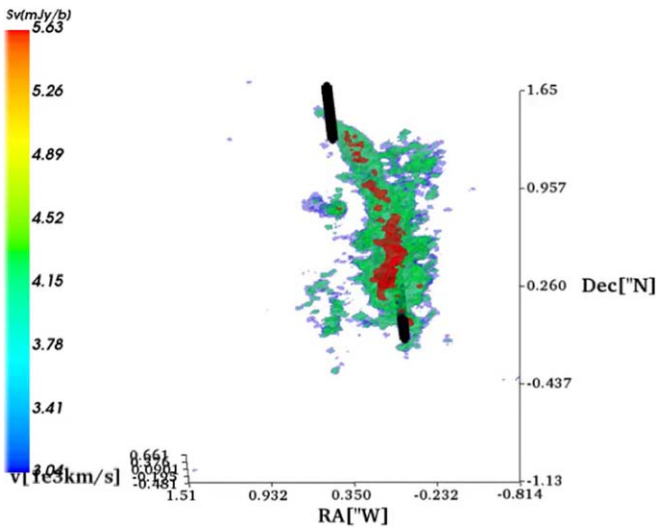


**Figure 4.** Still frame from the exploration of the ALMA data cube available as an animation in the electronic version of the journal. Three-dimensional axes show the spatial coordinates, R.A. and decl. relative to the center of the cube, and velocity in the line of sight. The black lines at all velocities show the positions of the north and south nuclei. The first 9 s of the animation rotate along the decl. axis. The next 5 s are about the R.A. axis, while the next 11 s are around the velocity axis. The final 4 s return the data cube to its original position. The majority of the gas in the central region is found on a filament connecting the two nuclei at a relatively constant velocity. Further, the decoupled structure at high velocity, described in Section 4.3, can be clearly seen in the animation.

(An animation of this figure is available.)

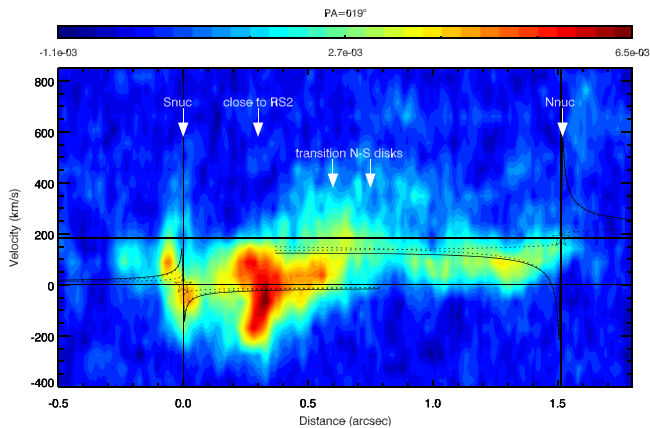


**Figure 5.** The  $p$ - $v$  diagram for the  $^{12}\text{CO}(2-1)$  emission along a PA of  $19^\circ$ , centered on the southern nucleus and passing through the northern one. The southern (at zero position and velocity) and northern (offset  $\sim 1''.5$  in position and  $\sim 182 \text{ km s}^{-1}$  in velocity) nuclei are marked by open stars. To guide the eye, vertical and horizontal lines mark the positions and recessional velocities, respectively, of the two nuclei. Also to guide the eye, we show for each nucleus the predictions of the velocity fields for the galaxy-only, black hole-only (dotted curves), and total (galaxy plus black hole) enclosed mass (solid curves; see text).

one could posit that the far side of the N stellar disk is to the southeast, as this overall orientation would most easily explain the observed internuclear bridge of gas. At offsets of  $0''.1$ – $0''.6$  northeast of the southern nucleus, the CO roughly follows the rotating stellar disk model of Medling et al. (2011), except for the high-dispersion region at offset  $\sim 0''.3$  north of the S nucleus. This structure is by far the most prominent feature seen in the  $p$ - $v$  diagram, as it includes the highest flux peak for the internuclear  $^{12}\text{CO}(2-1)$  emission and extends over

$400 \text{ km s}^{-1}$  in velocity space. It is strongly localized spatially, spanning roughly  $\sim 0''.2$ . This high-dispersion region is located at an offset where the slit passes very close to the radio supernova RS2 (which likely traces a starbursting region), detected at milliarcsecond-scale resolution in the radio by Hagiwara et al. (2011), and its peculiar molecular kinematics are discussed further below. At offsets between  $0''.9$  and  $1''.5$  north of the S nucleus, the gas roughly follows the predictions of the rotating northern stellar disk of Medling et al. (2015), though there are extra wiggles and a lack of Keplerian rotation inside the posited sphere of influence of the N nucleus black hole. Finally, at offsets between  $0''.5$  and  $0''.8$  north of the S nucleus, we see a clear transition region as the gas connects one of the claimed disks to the other. In summary, the gas bridge between the nuclei appears to connect them via the near side of the (behind) southern stellar disk and the far side of the (in front) northern one, and while some of the gas may be roughly consistent with the expected dynamics of the two nuclear core disks, there are clear streaming kinematics in the arm plus outflow signatures (in the S nucleus and near RS2) and a lack of Keplerian rotation near the N nucleus.

Figure 6 illustrates the projected geometry of the inner stellar disks and the CO emission, following the interpretation from Baan et al. (2007), based on H I absorption, placing the N disk in front of the S one. In this case, the relatively continuous velocity structure of the gas as it transitions between the two stellar disks (Figure 5) suggests that the disks intersect each other; i.e., the northeast of the S disk is the near side, and the southeast of the N disk is the far side. This is what we present in Figure 6. In this case, both the N and S disks are rotating counterclockwise on the sky. The east–west extension in CO in the area between the two nuclei likely traces the area where both disks actually intersect (rather than just overlap to our sight line). In the Baan et al. (2007) model, the radial distance between the two nuclei is  $\sim 3.3 \text{ kpc}$ , so the stellar disks illustrated in the figure would overlap by line-of-sight projection but not actually physically intersect. If this radial distance was decreased to  $< 2.4 \text{ kpc}$ , the two illustrated stellar disks would actually intersect over the ridgeline at which we see the maximum east–west extension of the CO emission.

There is significant evidence for symmetric superwind-driven outflows from the south nucleus (Heckman et al. 1990; Tecza et al. 2000; Baan et al. 2007). Our high-resolution molecular kinematics traces multiple outflow regions and shells. Figure 7 shows a  $p$ - $v$  diagram that crosses both the south nucleus and the location of the radio supernova RS2. As in Figure 5, we clearly see high-velocity dispersions around the location of RS2 (dotted vertical line). Further, even higher velocities are seen to the northeast of RS2 (larger positive offsets in the  $p$ - $v$  diagram). For illustration, we have overplotted the expected observed velocities from expanding spherical shells of gas with the expansion center at the southern nucleus (red) and the RS2 position (green). These are illustrative “toy” models fitted by eye; the true picture is certainly more complex, as the molecular gas is likely swept up from the internuclear bridge, which is likely highly inclined to our line of sight (see Section 1), and the shell morphology will depend strongly on the surrounding gas distribution with which it interacts. Further, the significantly different velocities required to explain the different shells in our toy model imply either that the periodic outflows are weakening over time or that we have ignored projection factors and local systemic

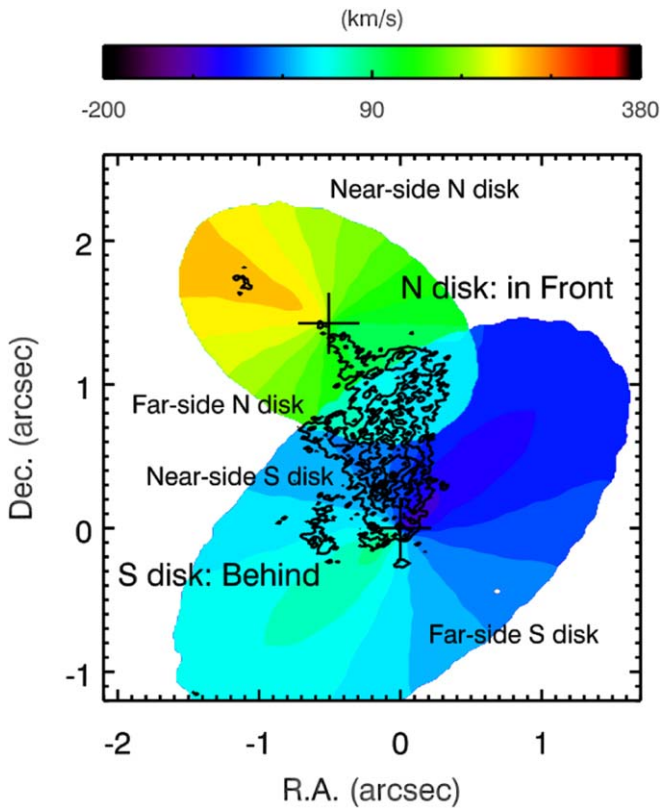


**Figure 6.** Illustration of the morphology and velocity (colors; following the color bar, in  $\text{km s}^{-1}$ , at the top; the color scale is binned at  $10 \text{ km s}^{-1}$ ) of the inner stellar disks of the N and S components in NGC 6240, with the integrated  $^{12}\text{CO}(2-1)$  emission overlaid with black contours. Nuclear positions are marked with plus signs. We follow the model of Baan et al. (2007), in which the N disk is closer to us and the S disk is further away. There appears to be a relatively continuous velocity structure traced by CO as the gas kinematics transitions from the S stellar disk to the N stellar disk. Figure 5 suggests that the two disks approach each other and perhaps interact. Based on this, we mark the near and far sides of each stellar disk. The N and S stellar disks shown are (for illustration)  $2''/2$  ( $\sim 1.1 \text{ kpc}$ ) and  $3''/8$  ( $1.9 \text{ kpc}$ ) in diameter. When the disks overlap (for our line of sight; note that this does not necessarily mean that they intersect, as discussed in the text), we show the average of the two disk velocities. The CO morphology appears to follow the line of overlap of the two disks, supporting a scenario in which they truly intersect. The best-fit stellar density profiles of Medling et al. (2015) are significantly different in the N and S stellar disks, with the former having a shallower ( $\rho \propto r^{-0.63}$ ) slope than the latter ( $\rho \propto r^{-1.5}$ ). This results in significantly different shapes for the stellar disk-only rotation curves in the two nuclei.

velocities. If the shells are comprised of gas swept up from the internuclear bridge, then the inclination of this bridge to the line of sight and the fact that the bridge’s systemic velocity gets more redshifted with larger offsets from the southern nucleus will both help to decrease the true difference in outflow velocities between shells. In any case, the dynamic timescales of these shells are significantly less than the estimated age of 10 Myr for the nuclear starburst (Tecza et al. 2000). As seen in Figure 7, the observed shells can be equally well explained as originating in either the southern nucleus or (near) RS2. However, there are two arguments that support an origin of the outflows from a region close to RS2. (1) The innermost shell extends over more than  $180^\circ$  in azimuth with a center very close to (but  $\sim 0''/02$  south of) RS2. If the outflow were driven by the south nucleus, we would expect the arc to be present only on the far side of RS2 (with respect to the southern nucleus). (2) If the shells originated in the southern nucleus, one would expect to see high-velocity arcs over a larger range

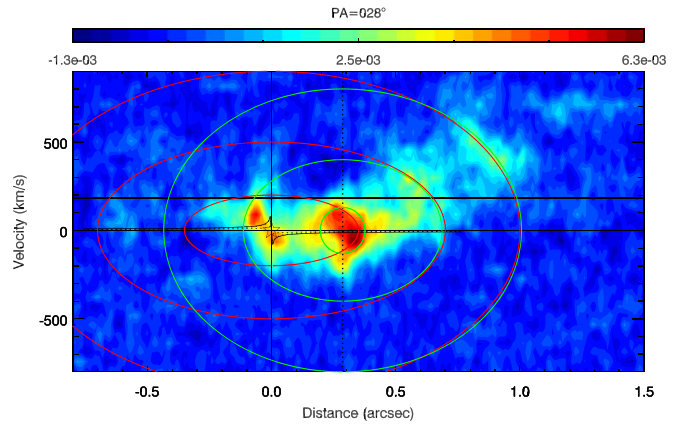


**Figure 7.** The  $p$ - $v$  diagram for the  $^{12}\text{CO}(2-1)$  emission along a PA of  $28^\circ$ , centered on the southern nucleus in position and velocity and passing through the radio supernova RS2 (at offset  $0''/3$ ). To guide the eye, horizontal lines delineate the recessional velocities of the N and S nuclei, and vertical lines delineate the positions of the S nucleus and RS2. Also to guide the eye, we show for the south nucleus the predictions of the velocity fields for the galaxy-only (top dashed curve), black hole-only (bottom dashed curve), and total (galaxy plus black hole) enclosed mass (solid curve; see the text). Ellipses delineate the expected observed velocities of radially expanding spherical shells around the south nucleus (red; velocities of 200, 500, and  $900 \text{ km s}^{-1}$  at radii of  $0''/35$ ,  $0''/7$ , and  $1''$ , respectively) and RS2 (green; velocities of 130, 400, and  $800 \text{ km s}^{-1}$  at radii of  $0''/09$ ,  $0''/4$ , and  $0''/72$ , respectively).

of offsets from the southern nucleus. What we observe, however, is that these are found at offsets consistent with them being driven out of the gas-rich region near RS2. Given that RS2 likely traces a more extended starburst region, a center slightly offset from RS2 is not unexpected.

The unusual kinematics in the sphere of influence of the south nucleus also deserves comment. Here, as in Figure 5, the velocities within  $\pm 0''/1$  of the southern nucleus do not follow those expected from the rotating model. Hagiwara et al. (2011) detected the young radio supernova RS1 35 mas southwest of the south nucleus. We note that the velocity pattern seen near the south nucleus appears symmetric about a negative offset (consistent with a shift toward the position of RS1) and a positive recessional velocity (consistent with the kinematics of the internuclear bridge) with respect to the southern nucleus. A detailed analysis of the outflows driven by RS1, RS2, S, and N are deferred to a forthcoming work.

We now analyze the kinematic properties of the molecular gas at larger scales by coarsely sampling the ALMA  $^{12}\text{CO}(2-1)$  SPW in  $26 \text{ km s}^{-1}$  bins. Figure 8 shows the detected  $^{12}\text{CO}(2-1)$  emission at four specific velocities relative to the systemic velocity of the system, defined to be that of the southern nucleus:  $-148.2$  (blueshifted stream),  $7.9$  (systemic),  $164.0$  (redshifted stream), and  $528.1$  (outflowing material)  $\text{km s}^{-1}$ . Most of the blueshifted material is found near the southern part of the stream, while the redshifted emission is seen near the northern end. This suggests that the stream can be considered as a dynamic structure that is interacting with and evolving relative to the two nuclei.

### 3.4. Velocity Dispersion

The velocity dispersion, in particular relative to the kinematical structure of the system, provides important clues about the dynamical state of the molecular gas in the nuclear regions of this system. Previous observations, such as those presented by Feruglio et al. (2013b), found that at lower,  $\sim 1''$ ,

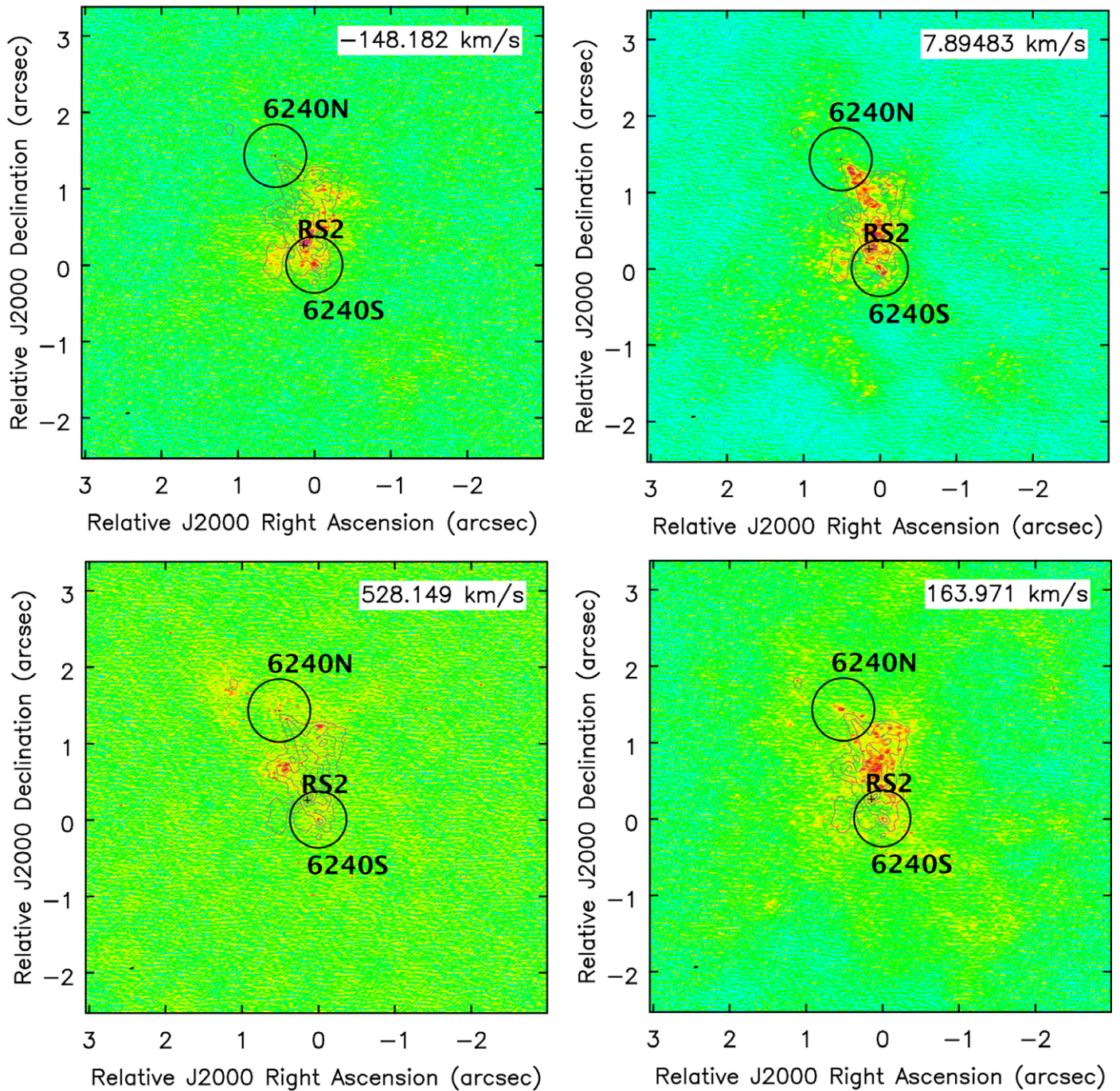


**Figure 8.** The  $^{12}\text{CO}(2-1)$  emission as measured by ALMA in NGC 6240 in four channel maps:  $-148.2$  (blueshifted stream; top left panel),  $7.9$  (systemic; top right panel),  $164.0$  (redshifted stream; bottom right panel), and  $528.1$  (outflowing material; bottom left panel)  $\text{km s}^{-1}$ . The gray contours in all panels show the integrated  $^{12}\text{CO}(2-1)$  emission, as shown in Figure 1. Each contour shows an increase of 20% in flux starting from a base level of  $0.2 \text{ Jy beam}^{-1} \text{ km s}^{-1}$ . The black circles have radii of  $\sim 200$  pc centered on the position of the VLBI emission.

spatial resolutions, velocity dispersions fell within the range  $\sim 150\text{--}300 \text{ km s}^{-1}$  but reached up to  $\sim 500 \text{ km s}^{-1}$  in the region between the nuclei and around the northern center. Our ALMA observations, shown in Figure 9, find consistent results, with typical velocity dispersion values in the region between the nuclei of  $\sim 130\text{--}150 \text{ km s}^{-1}$  and higher values, reaching  $\sim 250 \text{ km s}^{-1}$ , mostly along the edges of the internuclear CO emission. In the northern nucleus, using a radius of  $\sim 200$  pc, we find an average velocity dispersion of  $184 \text{ km s}^{-1}$ , while for the southern one, in a similar area, we find an average velocity dispersion of  $155 \text{ km s}^{-1}$ . These values are significantly lower

than those reported by Feruglio et al. (2013b) and highlight how the spatial resolution of the two observations,  $\sim 1''$  versus  $\sim 0''.03$ , plays a crucial role in the interpretation of the gas state near the SMBHs. Indeed, SMA observations of the  $^{12}\text{CO}(3-2)$  line carried out by U et al. (2011) at a resolution of  $\sim 0''.3$  similarly find a modest velocity dispersion for the molecular gas, fully consistent with what is reported here. Comparable values were also found from ALMA observations of the [C I] (1-0) line emission reported by Ciccone et al. (2018).

Albeit lower than previously reported, these still relatively high velocity dispersion values imply  $v/\sigma \sim 1$  and hence

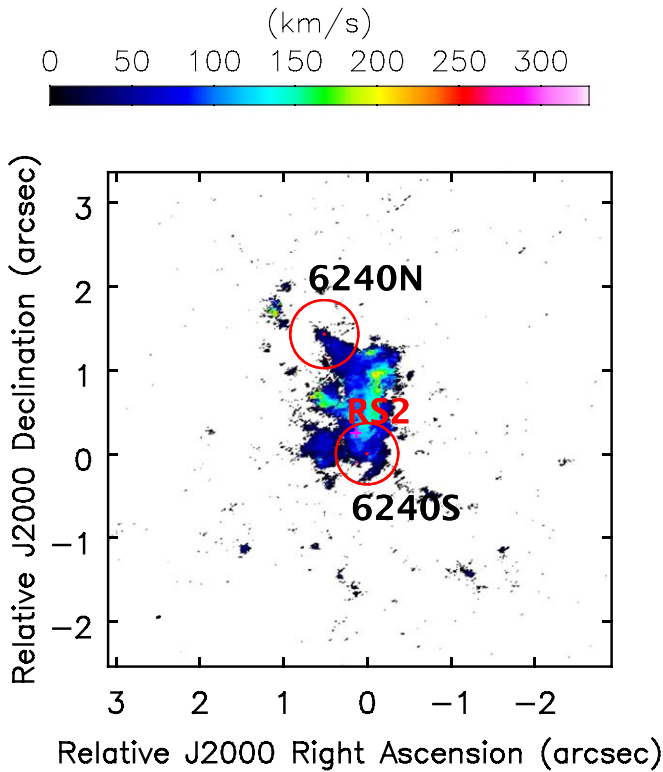


**Figure 9.** Velocity dispersion map for the molecular gas in NGC 6240, as traced by ALMA using the  $^{12}\text{CO}(2-1)$  emission line. The red circles have radii of  $\sim 230$  pc, roughly the sphere of influence for each SMBH, centered on the position of the VLBI emission (magenta dots), while the magenta plus sign marks the position of RS2.

suggest that the kinematics of the internuclear gas is dominated by turbulence, possibly associated with the presence of significant shocks in the internuclear molecular gas. In addition, and as presented by U et al. (2011), the velocity dispersion distribution is not connected to the overall velocity gradient between the nuclei. This latter fact would indicate that the bulk of the molecular gas, traced by the CO emission, is not undergoing organized circular movements, as proposed previously (e.g., Engel et al. 2010), but instead is consistent with being dynamically supported by turbulence. This seems natural if this is indeed a transient structure created by the merger, which, after a relatively short time (compared to the duration of the merger), may (at least partially) collapse around the new coalesced center of the system, as was previously discussed by Engel et al. (2010) and others and predicted by numerical simulations (Bournaud et al. 2011).

#### 4. Discussion

##### 4.1. Gas Mass from $^{12}\text{CO}(2-1)$

While  $\text{H}_2$  is the most abundant molecule in galaxies, it cannot be directly observed in emission due to its lack of dipolar rotational transitions at relatively low excitation temperatures (Bolatto et al. 2013, and references therein). In contrast, the CO molecule can be easily excited even in cold environments and is relatively abundant, making it an important tracer of the molecular gas contents of a galaxy. In order to convert from observed  $^{12}\text{CO}(2-1)$  line flux to total molecular gas mass, we follow the procedure described by Solomon & Vanden Bout (2005), as was done previously by

Treister et al. (2018). Specifically, the line luminosity is computed from the observed line flux as

$$L'_{\text{CO}} = 3.25 \times 10^7 S_{\text{CO}} \Delta\nu \nu_{\text{obs}}^{-2} D_L^2 (1+z)^3.$$

From the line luminosity, we estimate the molecular hydrogen mass as

$$M(\text{H}_2) = \alpha_{\text{CO}} L'_{\text{CO}},$$

where  $\alpha_{\text{CO}}$  is the CO-to- $\text{H}_2$  conversion factor. Then, by incorporating the He contribution into this factor, we obtain the total molecular gas mass. The value of  $\alpha_{\text{CO}}$  and its possible variations for different galaxies, and even regions inside a galaxy, are topics still extensively debated in the literature (e.g., Bolatto et al. 2013). The value typically assumed for galaxies like the Milky Way is  $4.6 M_{\odot} (\text{K km s}^{-1} \text{pc}^2)^{-1}$  (Bolatto et al. 2013). However, in extreme environments, such as those observed in (U)LIRGs, lower  $\alpha_{\text{CO}}$  values of  $\sim 0.6-1 M_{\odot} (\text{K km s}^{-1} \text{pc}^2)^{-1}$  have been reported (e.g., Downes & Solomon 1998; Tacconi et al. 2008; Yamashita et al. 2017; Herrero-Illana et al. 2019), likely associated with higher velocity dispersions (Papadopoulos et al. 2012). For a source as complex as NGC 6240, it is dangerous to assume a single value of  $\alpha_{\text{CO}}$ , as previously argued by Engel et al. (2010). Previously, for this galaxy, Tunnard et al. (2015) reported a very broad range of  $\alpha_{\text{CO}}$  values spanning up to 3 orders of magnitude, from  $\sim 0.1$  to  $\sim 100 M_{\odot} (\text{K km s}^{-1} \text{pc}^2)^{-1}$  (see their Figure 10, left panel). However, the reported range in the global value of  $\alpha_{\text{CO}}$  is much narrower, finding  $\alpha_{\text{CO}} = 1.5_{-1.1}^{7.1} M_{\odot} (\text{K km s}^{-1} \text{pc}^2)^{-1}$ . In parallel, using combined observations of HCN, CS, and  $\text{HCO}^+$  transitions, Papadopoulos et al. (2014) estimated a conversion factor of  $\alpha_{\text{CO}} = 2-4 M_{\odot} (\text{K km s}^{-1} \text{pc}^2)^{-1}$ . More recently, based on ALMA observations at lower spatial resolutions than those presented here, Cicone et al. (2018) reported a mean value of  $\alpha_{\text{CO}} = 3.2 \pm 1.8 M_{\odot} (\text{K km s}^{-1} \text{pc}^2)^{-1}$  for the systemic components and  $\alpha_{\text{CO}} = 2.1 \pm 1.2 M_{\odot} (\text{K km s}^{-1} \text{pc}^2)^{-1}$  for the outflowing material (presented in their Table 2). We adopt the Cicone et al. (2018)  $\alpha_{\text{CO}}$  conversion factor for our calculations, together with their values of  $r_{21} = 1.0 \pm 0.2$  for the systemic component and  $1.4 \pm 0.3$  for the outflows, where  $r_{21}$  is defined as the ratio between the  $^{12}\text{CO}(2-1)$  and  $^{12}\text{CO}(1-0)$  luminosities. When comparing to previous results, it is important to consider that fiducial values of  $\alpha_{\text{CO}} = 1 M_{\odot} (\text{K km s}^{-1} \text{pc}^2)^{-1}$  were typically assumed (e.g., Engel et al. 2010).

We adopt three distinct regions: the spheres of influence of the northern and southern SMBHs and a  $1''$  diameter aperture centered equidistantly along the line connecting the two nuclei ( $16^{\text{h}}52^{\text{m}}58.896$ ,  $02^{\circ}24'03''.96$ ). The velocity-integrated  $^{12}\text{CO}(2-1)$  flux measurements are  $34.3 \pm 3.7$ ,  $142.1 \pm 3.1$ , and  $389 \pm 11 \text{ Jy km s}^{-1}$ , respectively. The central  $1''$  flux density is similar, albeit  $\sim 25\%$  smaller, to the one reported by Tacconi et al. (1999), which might indicate that our interferometric observations may have resolved out a small fraction of the internuclear molecular mass; however, the lower-resolution value of Tacconi et al. (1999) likely includes substantial flux from the nuclei, at least partially accounting for the 25% difference. The fluxes for the two nuclei are fully consistent with those measured previously by Engel et al. (2010). As presented in Section 3, considering a much larger aperture of  $25''$  in diameter that should include most of the source

$^{12}\text{CO}(2-1)$  emission, we measure a flux of  $1163 \pm 28 \text{ Jy km s}^{-1}$ , consistent with the  $1220 \text{ Jy km s}^{-1}$  reported by Tacconi et al. (1999) and the  $\sim 1000 \text{ Jy km s}^{-1}$  inferred from the  $^{12}\text{CO}(1-0)$  observations by Solomon et al. (1997).

Using the expressions derived above, these line fluxes correspond to gas masses of  $7.4 \times 10^8 M_\odot$  for the northern nucleus,  $3.3 \times 10^9 M_\odot$  for the southern nucleus, and  $8.6 \times 10^9 M_\odot$  for the central region. This is consistent with the values previously derived by Engel et al. (2010) and Feruglio et al. (2013b), once the differences in the assumed values of  $\alpha_{\text{CO}}$  are accounted for. Finally, from the computed total flux in the  $25''$  diameter aperture, we derive a mass of  $2.6 \times 10^{10} M_\odot$ . This is fully consistent with the value of  $(2.1 \pm 0.5) \times 10^{10} M_\odot$  reported by Cicone et al. (2018) in a central  $12'' \times 6''$  region.

The total molecular gas mass can also be estimated from the warm molecular gas, as presented by Dale et al. (2005), even considering that the latter is not a direct tracer of the cold molecular gas. Specifically, for our comparison, we can use the  $\text{H}_2(1-0 \text{ S}(1))$  line luminosity at rest frame  $2.12 \mu\text{m}$ . We use the empirically calibrated relation  $L_{(1-0)\text{S}(1)}/M_{\text{gas}} = 2.5 \times 10^{-3}$ , as measured specifically for NGC 6240 by Müller Sánchez et al. (2006). This luminosity can be estimated from the VLT/SINFONI observations of NGC 6240 presented by Engel et al. (2010). Using a nuclear  $2''$  diameter aperture, we estimate an  $L_{(1-0)\text{S}(1)}$  luminosity of  $2.8 \times 10^7 L_\odot$ , or, equivalently,  $1.1 \times 10^{10} M_\odot$ , and hence fully consistent with the values derived here based on the  $^{12}\text{CO}(2-1)$  observations. The comparison of the results obtained using the empirically calibrated  $L_{(1-0)\text{S}(1)}/M_{\text{gas}}$  ratio with the new ALMA observations presented in this paper indicates that we can use the  $\text{H}_2(1-0 \text{ S}(1))$  line to make at least an approximate estimate of the total (cold) molecular gas mass.

#### 4.2. Gas Mass from Submillimeter Continuum

In the past, most studies of the ISM in the molecular gas phase have relied on the rotational transitions of the CO molecule to trace  $\text{H}_2$  gas. However, as shown by Scoville et al. (2014, 2016), measurements of the dust continuum emission at the long-wavelength Rayleigh–Jeans (RJ) end can also provide accurate estimates of the ISM mass in a small fraction of the required observing time with ALMA. At these long wavelengths, the dust emission is thought to be optically thin; hence, the observed continuum flux density is directly proportional to the mass once the dust opacity coefficient and dust temperature are established. It is important to point out that this estimation depends on the assumption that the continuum emission at these wavelengths is dominated by thermal dust radiation, which might not be the case in the central region of NGC 6240. Evidence in this direction was presented by Tacconi et al. (1999) and later by Nakanishi et al. (2005) based on the observed spectral slope, which is consistent with that expected for synchrotron radiation. In addition, Meijerink et al. (2013) argued that the CO-to-continuum luminosity ratio in this galaxy is significantly larger than the value observed in other similar systems, which might be an indication of significant shock heating. However, as was presented by Medling et al. (2019), the estimated synchrotron emission in the northern and southern nuclei is 0.16 and 0.08 mJy, respectively, and hence negligible compared to the observed continuum fluxes reported in Section 3.2. Therefore, we can assume that the continuum emission is dominated by thermal emission from dust and hence compare this estimate to the molecular gas mass derived

in the previous section. Following the procedure presented by Scoville et al. (2015), the ISM mass is given by their Equation (3):

$$M_{\text{ISM}} = \frac{0.868 \times S_\nu (\text{mJy}) d_{\text{Gpc}}^2}{(1+z)^{4.8} T_{25} \nu_{350}^{3.8} \Gamma_{\text{RJ}}} 10^{10} M_\odot,$$

where  $\Gamma_{\text{RJ}}$  is a correction factor that accounts for the departure from the RJ regime and is given by

$$\Gamma_{\text{RJ}} = 0.672 \times \frac{\nu_{350}(1+z)}{T_{25}} \times \frac{1}{e^{0.672 \times \nu_{350}(1+z)/T_{25}} - 1}.$$

For our observations of NGC 6240,  $\nu_{\text{obs}}$  corresponds to 235 GHz, or 0.67 in  $\nu_{350}$  units;  $z = 0.02448$ ; and  $d_{\text{Gpc}} = 0.1$ . Furthermore, we assume  $T_{25} = 1$ . From the ALMA compact and intermediate configuration Band 6 continuum maps of the southern and northern nuclei, as defined by the radius of the SMBH sphere of influence, we measure 235 GHz continuum fluxes of  $5.19 \pm 0.06$  and  $1.73 \pm 0.03$  mJy, respectively, as presented in Section 3.2. These correspond to ISM masses of  $2.1 \times 10^9$  and  $6.9 \times 10^8 M_\odot$ , respectively. These masses are roughly consistent with those derived from the CO measurements in the previous section. Differences of that order are expected, given the typical uncertainties in the assumed values of  $\alpha_{\text{CO}}$  and  $T_{25}$ , that cannot be determined directly from our ALMA data at these high resolutions.

To determine if the difference in molecular mass estimations could be caused by a surface brightness sensitivity issue, we use the Scoville et al. (2016) relation to calculate the expected  $850 \mu\text{m}$  luminosity from the CO-derived molecular mass within the central  $2''$  aperture. We then convert this luminosity to an equivalent 235 GHz continuum emission (again assuming  $\beta = 1.8$ ) and estimate the flux density per beam in our long baseline observations. We find that the predicted dust continuum emission per beam associated with the CO-detected molecular concentration in the internuclear  $1''$  region is an order of magnitude fainter than the sensitivity of our observations. This indicates that dust-based ISM mass estimates can be biased low in situations where galaxies are highly resolved.

#### 4.3. Outflowing Material

The velocity map presented in Figure 3 shows a high-velocity,  $>500 \text{ km s}^{-1}$ , component separated by  $\sim 400$  pc in projection to the south of the northern nucleus. A map showing the structure of this high-velocity material is presented in Figure 10. There seems to be a faint bridge of gas extending back to the northern nucleus. This structure was also presented and studied by Feruglio et al. (2013b) and later by Saito et al. (2018) from lower-resolution  $^{12}\text{CO}(2-1)$  observations. More recently, Cicone et al. (2018) reported the detection of this nuclear outflow in the  $\text{CO}(1-0)$ ,  $\text{CO}(2-1)$ , and  $[\text{C I}](1-0)$  transitions, and Müller-Sánchez et al. (2018) reported it in  $\text{H}_2$ . Given its high velocity, we speculate that this is an outflow of molecular gas expelled from the nuclear region of the merger system. The total mass of this outflowing material is estimated at  $9 \times 10^8 M_\odot$ , considering the  $\alpha_{\text{CO}}$  factor computed specifically for the outflowing material by Cicone et al. (2018). This is very significant, as it represents  $\sim 3.5\%$  of the total molecular gas in the system and  $10.5\%$  of the molecular mass in the central region. If we assume that it is linked to the

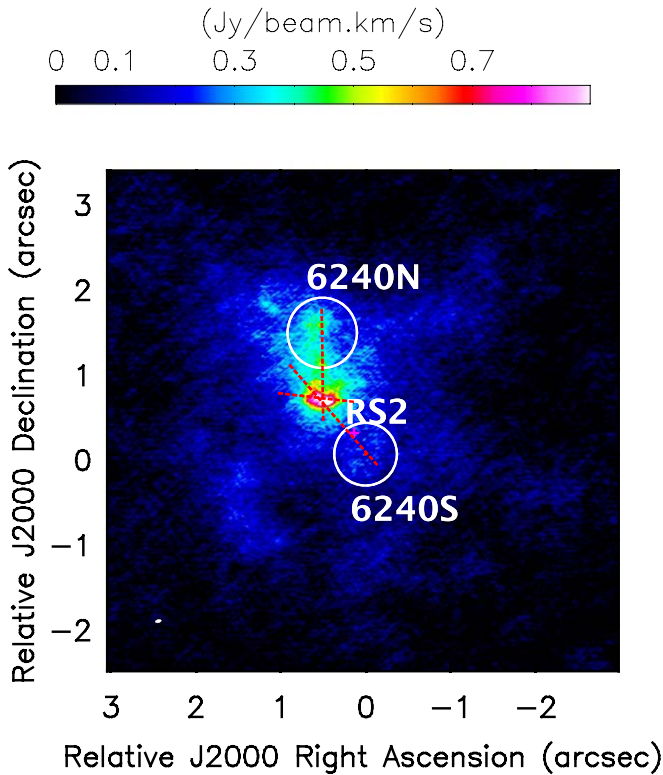


**Figure 10.** ALMA moment 0 map of the  $^{12}\text{CO}(2-1)$  emission at relative velocities greater than  $500 \text{ km s}^{-1}$ . Symbols are the same as in Figure 3. A clear high-velocity emission concentration is visible directly to the south of the northern nucleus. This emission appears to be connected to the northern nucleus by a fainter emission bridge. Three  $p-v$  diagrams, presented in Figure 11, were extracted to characterize the high-velocity structure, as shown by the dotted red lines.

northern nucleus and has been moving at a constant speed, this material would have been expelled at least 0.78 million yr ago.

We estimate the mass outflow rate associated with this high-velocity structure using Equation (3) of Maiolino et al. (2012),

$$\dot{M}_{\text{out}} = 3v \frac{M_{\text{out}}}{R_{\text{out}}},$$

where  $v$  is a representative velocity of the wind,  $M_{\text{out}}$  is its mass, and  $R_{\text{out}}$  is its size. This equation assumes a relatively simple geometry for the outflow, given by a spherical or, equivalently, conical or multiconical volume uniformly filled by outflowing clouds. We caution that the geometry of this outflow is likely more complex, and hence the values derived using this expression have uncertainties of factors of  $\sim 3$  (Lutz et al. 2020). Assuming values of  $v = 500 \text{ km s}^{-1}$ ,  $M_{\text{out}} = 9 \times 10^8 M_{\odot}$  and  $R_{\text{out}}$  between 290 and 430 pc, depending on whether the wind arises from the northern nucleus for the latter or the extension of the high-velocity structure for the former. We then obtain values of  $3200\text{--}4700 M_{\odot} \text{ yr}^{-1}$ , roughly consistent with the value of  $2500 \pm 1200 M_{\odot} \text{ yr}^{-1}$  reported by Cicone et al. (2018).

We can then constrain the ultimate fate of the wind by comparing the wind velocity with the system’s escape velocity. The stellar mass of NGC 6240 is  $3.9 \times 10^{11} M_{\odot}$  (Howell et al. 2010); with the abundance matching of Moster et al. (2010), the predicted halo mass is  $\sim 12 \times 10^{14} M_{\odot}$ . The escape velocity for a halo of this mass is  $\sim 1000 \text{ km s}^{-1}$ , computed at

$R_{200}$  ( $\sim 1 \text{ Mpc}$ ). Assuming there is no further injection of energy, most of the mass will remain bound to the halo. If the material in the wind is efficiently heated and joins the X-ray halo (Nardini et al. 2013), future star formation may be delayed or prevented as a result of the wind’s removal of material from the center of NGC 6240. The presence of this high-speed massive clump implies a very efficient process capable of accelerating high-velocity massive amounts of material and, consequently, due to the gas reservoir removal, significantly diminishing or even shutting down nuclear star formation episodes triggered by the major galaxy merger. Taking the previously derived total molecular gas mass of  $2.6 \times 10^{10} M_{\odot}$  and the outflow rate of  $3200 M_{\odot} \text{ yr}^{-1}$ , the implied gas removal time by the wind alone is 8.1 Myr.

In order to explore the kinematic properties of the aforementioned high-velocity material, in Figure 11, we present three  $p-v$  diagrams: one along the bulk of the high-velocity emission, roughly in the east–west direction; another tracing the material bridging this cloud to the northern nucleus, roughly oriented north–south; and another connecting the high-velocity emission to the southern nucleus, as shown in Figure 10. No evidence of rotation or obvious kinematic structures can be seen in the high-velocity emission. This emission extends from  $\sim 300$  to  $\sim 800 \text{ km s}^{-1}$ , spanning  $\sim 0''.3$  in size, which corresponds to  $\sim 150 \text{ pc}$  in projection at the distance of NGC 6240. The north–south  $p-v$  diagram (middle panel of Figure 11) shows a rather steep gradient, which might be indicative of, for example, an expanding shell. A faint connecting bridge can be observed in Figure 10 between the northern nucleus and the high-velocity structure. This emission can also be seen in the middle panel of Figure 11 at a relatively constant velocity of  $\sim 600 \text{ km s}^{-1}$  and spanning spatial offsets between  $0''.2$  and  $0''.6$ , almost reaching the northern nucleus. No similar connection can be seen relative to the southern nucleus (bottom panel of Figure 11). As reported by Müller-Sánchez et al. (2018), the high-velocity outflow is clearly detected in the  $\text{H}_2$  VLT/SINFONI map and spatially coincident [O III] emission, as observed in *HST* Wide Field Camera 3 (WFC3) maps of the region. Considering as well the lack of  $\text{H}\alpha$  emission at this location, also reported by Müller-Sánchez et al. (2018), the physical origin of this structure remains uncertain. Given its complexity, a full kinematic analysis of this high-velocity structure and the models for its origin are beyond the scope of this paper.

#### 4.4. Molecular Gas as Fuel for Star Formation

As shown by Medling et al. (2015), both SMBHs are currently more massive than expected based on the black hole mass–galaxy property correlations, requiring an increase in the total stellar mass of  $1.7 \times 10^{11} M_{\odot}$  to reach the scaling relation. Assuming that all of the molecular gas currently in the sphere of influence of each SMBH will be accreted by them, the SMBHs would only grow by  $\sim 45\%$  and hence not change too much in overall mass in the short term. The total mass reservoir is, however, significantly larger, considering the  $\sim 9 \times 10^9 M_{\odot}$  of molecular gas in the central  $1''$  (500 pc) diameter inferred from the ALMA  $^{12}\text{CO}(2-1)$  observations. Its precise fate, whether to be accreted, form stars, or be expelled from the system through outflows, is highly uncertain at this point. However, recent observations of a similar system, Mrk 463 (Treister et al. 2018), show that only a very small fraction,  $< 0.01\%$ , of the available mass is actually being accreted by the

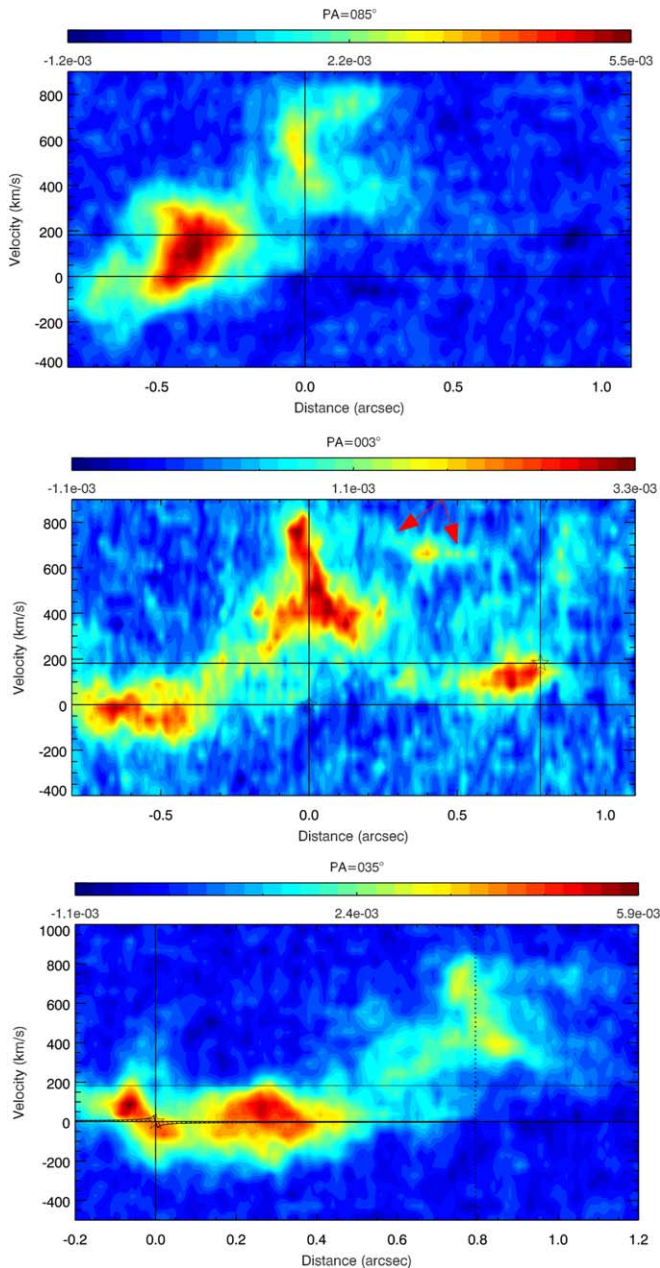


**Figure 11.** The  $p$ - $v$  diagrams specifically tracing the high-velocity emission shown in Figure 10. The top panel shows a diagram along the brightest axis of the emission, at a PA of  $85^\circ$ , roughly aligned in the east–west direction, while the middle panel shows a cut along the fainter material connecting the northern nucleus to the center of the high-velocity emission, roughly in the north–south direction, at a PA of  $3^\circ 3$ . The bottom panel presents the  $p$ - $v$  diagram from the high-velocity emission to the southern nucleus at a PA of  $35^\circ$ . In the top and middle panels, the vertical line at an offset of  $0''$  marks the center of the high-velocity emission, while in the bottom panel, the southern nucleus is at an offset of  $0''$  and the high-velocity emission is at  $\sim 0''.8$ . No well-defined kinematic structure can be seen in the region of the high-velocity emission. The faint emission connecting the high-velocity structure to the northern nucleus seen in Figure 10 is visible in the middle panel at a velocity of  $\sim 600 \text{ km s}^{-1}$  and offsets between  $0''.2$  and  $0''.6$ , indicated by the red arrows.

SMBHs. Therefore, we could expect that, after subtracting the outflowing material, most of the remaining molecular gas will be used as fuel for star formation. Assuming typical efficiencies for star formation for giant molecular clouds of  $\sim 1\%$ – $10\%$  (Murray 2011; Ochsendorf et al. 2017), this implies an expected increase of the stellar mass in the nuclear region of

$(0.3\text{--}3) \times 10^8 M_\odot$ , which is certainly not enough to make the resulting system consistent with the observed black hole–stellar mass correlation. Even if all of the molecular gas in the system is considered, these conclusions are not altered significantly, even if much higher star formation efficiencies are invoked.

## 5. Conclusions

The unprecedented high-resolution ALMA observations of the molecular gas in the merging system NGC 6240 allow us to pin down how SMBH growth and star formation are proceeding in this complex and chaotic environment. While previous observations of these and other nearby major galaxy mergers reached spatial resolutions of  $100\text{--}1000 \text{ pc}$ , the recent availability of ALMA configurations reaching  $>10 \text{ km}$  baselines allowed us to sharpen this view by an order of magnitude. This allows us to resolve scales comparable to the sizes of average giant molecular clouds (Murray 2011) and hence measure the size, mass, and kinematics for many active sites of nuclear star formation. Therefore, and as we have shown here, we can now study the properties of the gas inside the sphere of influence of each SMBH that is readily available to feed them, quantify the general kinematic structure of the gas, and identify high-velocity outflows.

Specifically for NGC 6240, the high-resolution Band 6 ALMA observations of the  $^{12}\text{CO}(2\text{--}1)$  emission have confirmed that the bulk of the nuclear molecular gas,  $\sim 9 \times 10^9 M_\odot$ , is located in an  $\sim 1''$  ( $470 \text{ pc}$ ) region between the two nuclei. Significant amounts of molecular gas,  $7.4 \times 10^8$  and  $3.3 \times 10^9 M_\odot$  in the northern and southern nuclei, respectively, are found inside the sphere of influence of each SMBH. Contrary to previous lower spatial resolution observations, we do not find evidence for a kinematic rotating disk between the two nuclei. Instead, we find two spatially localized velocity gradients reaching  $\sim 200$  and  $\sim 400 \text{ km s}^{-1}$ , both in the surroundings of the southern nucleus. We find further evidence for a very significant,  $\sim 11\%$  of the nuclear molecular mass, high-velocity,  $>500 \text{ km s}^{-1}$ , outflow. Its origin is not clear but could be connected and physically linked to the northern nucleus. Studying the velocity dispersion, we find that the general dynamics of the molecular gas are consistent with being dominated by turbulent or disordered motions and high-velocity winds, most likely related to the ongoing major galaxy merger and nuclear activity. While the final fate of this molecular mass cannot be determined, it is expected that a fraction of it will eventually feed both SMBHs, which are currently above the well-established black hole mass–stellar mass correlation. This offset will not disappear, even if a significant fraction of the molecular mass in the nuclear region is converted into stars at typical efficiencies. Major galaxy mergers are relatively rare, particularly in the local universe, with only a few tens close enough and bright enough to carry out such sensitive high-resolution observations. It is particularly important to be able to carry out this high-resolution analysis for a sample of sources spanning different merger stages in order to be able to establish the evolution of the molecular gas across the merging sequence, a process that should take an average of  $1\text{--}2 \text{ Gyr}$ .

We thank the anonymous referee for a very constructive review of this article. We acknowledge support from FONDECYT Regular 1160999 (E.T.), 1190818 (E.T., F.E. B.), CONICYT PIA ACT172033 (E.T., N.N.), Basal-CATA

PFB-06/2007 (E.T., F.E.B., N.N.), and AFB170002 (E.T., F.E.B., G.V., N.N.) grants and Chile’s Ministry of Economy, Development, and Tourism’s Millennium Science Initiative through grant IC120009, awarded to the Millennium Institute of Astrophysics, MAS (F.E.B.). G.C.P. acknowledges support from the University of Florida. C.C. acknowledges funding from the European Union Horizon 2020 research and innovation program under Marie Skłodowska Curie grant agreement No. 664931. This work was performed in part at the Aspen Center for Physics, which is supported by National Science Foundation grant PHY-1607611. This paper makes use of the following ALMA data: ADS/JAO.ALMA#2015.1.00370.S and #2015.1.00003.S. ALMA is a partnership of the ESO (representing its member states), NSF (USA), and NINS (Japan), together with the NRC (Canada), MOST and ASIAA (Taiwan), and KASI (Republic of Korea), in cooperation with the Republic of Chile. The Joint ALMA Observatory is operated by the ESO, AUI/NRAO, and NAOJ. The National Radio Astronomy Observatory is a facility of the National Science Foundation operated under cooperative agreement by Associated Universities, Inc.

*Facility:* ALMA.

## Appendix ALMA Array Setup and Data Analysis

### *A.1. Compact and Intermediate Configurations*

The initial calibration of the short baseline ( $\lesssim 1$  km) had some slight changes in EBs Xb4da9a/X69a and Xb5fdce/X79d. In the former, the spectral slope of J1550+0527, derived based on the Titan amplitude solutions, was considered in order to obtain an improved bandpass solution. In the latter, J1751+0939 was used as a flux calibrator instead of Pallas, which showed problematic amplitude visibilities inducing a general overestimate of the sources’ fluxes. Also, despite the short times on source (1–4 minutes), a single self-calibration step considering phase solutions alone was adopted (no major improvement was found by considering the amplitude solutions). This was done by setting the solution interval parameter to “inf” and not adopting any scan average. Since each scan was  $\sim 50$ –60 s long, in practice, this was the time range used.

Figure 12 shows the amplitude versus  $uv$  distance visibility distribution for the pointlike calibrators used for flux, bandpass, or phase calibration, as well as the check sources. One can see that J1751+0939 shows modest large-scale structure being picked up by the shortest baselines ( $\lesssim 50$  k $\lambda$ ), but this difference is about 1% above the core emission and thus is not expected to affect the calibration. Both J1550+0527 and J1751+0939 show visible variability in either flux, slope, or polarization. Comparing to the AMAPOLA<sup>27</sup> database, which makes use of ALMA’s Grid Survey observations, one can see that J1550+0527 shows flux variability at the 10%–18% level from 2016 January to June and an increase of polarized flux in the same period. As for J1751+0939, there is an even larger variation in the flux and polarization fractions during the period of observations, with a peak in the first half of 2016 July (Xb5fdce/X79d). The fact that J1751+0939 was used as a flux calibrator in the execution Xb5fdce/X79d, which shows the highest flux density, does not affect the calibration. In fact, both

J1651+0129 and J1659+0213, whose amplitude and bandpass calibrations depend on the previous sources, do not show the same flux and polarization fraction variations or any correlation. This indicates that the variation in J1751+0939 on that day was due to intrinsic source variability.

Likewise, we also display in Figure 13 the phase versus  $uv$  distance for the same sources. All of the sources in these configurations show scatter around  $0^\circ$  with no obvious trend with increasing baseline length, demonstrating that these sources are pointlike and have been observed at the phase center. Here J1550+0527 and J1751+0939 always show a phase scatter below  $1^\circ$ , while the phase calibrator J1651+0129 always appears below  $10^\circ$ , implying that the signal decorrelation is smaller than 1.5% ( $\epsilon \equiv e^{-\sigma_\phi^2/2}$ , where  $\sigma_\phi$  is the phase rms in radians).

### *A.1.1. High Resolution*

Two visits were executed with the longest-baseline configuration. Both used J1651+0129 ( $1^\circ 02'$  away) as a phase calibrator. The 2015 (Xac5575/X8a5f) visit was executed under poor phase stability ( $\sigma_\phi \sim 47^\circ$ ), resulting in strong signal decorrelation, while the second one, in 2017 (Xc5148b/X127e), had better phase stability ( $\sigma_\phi \sim 13^\circ$ ), even though it was still marginal (phase rms at longer baselines of  $40^\circ$ – $70^\circ$ ). This could be concluded from the dynamic range (DR) obtained in the continuum image of our scientific target, NGC 6240, resulting from the two executions. Although both observations have comparable noise levels ( $\sim 29 \mu\text{Jy beam}^{-1}$ ), we find peak fluxes of the southern nucleus of 673 (DR = 24) and 2984 (DR = 102)  $\mu\text{Jy}$  in Xac5575/X8a5f and Xc5148b/X127e, respectively. Assuming this nucleus presented no significant flux variability within the time separating the two observations, this signal decorrelation is quite critical.

For this reason, we considered the use of the algorithm developed by Maud et al. (2017), which, based on the bandpass scan, finds the best water vapor radiometer (WVR) solution scaling to account for the dry component in the atmosphere. We note that one should expect small changes, since these observations were conducted under  $\text{PWV} \sim 1$ , the upper limit where this scaling is expected to induce significant changes. The assessment of its application was done in two ways: determining the DR of the NGC 6240 continuum image (dominated by the two pointlike nuclei) and the improvement of the phase rms in each antenna in the phase-calibration and check-source scans. When applying the scaling to these data sets, we retrieve noise levels of 24 and 28  $\mu\text{Jy beam}^{-1}$  for Xac5575/X8a5f and Xc5148b/X127e, respectively. The peaks are now found to be 805 (DR = 33;  $5.5\sigma$  increase) and 3031 (DR = 108;  $1.7\sigma$  increase)  $\mu\text{Jy beam}^{-1}$ , respectively. The DR increase in the latter is small, but we decided to keep this scaling, since the phase rms improved for most antennas (41 out of 43 in the phase-calibrator scans and 31 out of 43 in the check-source scans). Given the significant difference between the two data sets, the final images consider the Xc5148b/X127e alone, which is less affected by signal decorrelation.

Further assessing the data quality in Xc5148b/X127e, we focus on the check source (J1649+0412). This is expected to be pointlike, but after applying the phase solutions based on the phase calibration (J1651+0129,  $2^\circ 74'$  away), it appears to be slightly extended. The integrated-to-peak flux ratio is  $\sim 1.5$  (190 versus 130 mJy), and the phase rms is  $\sim 40^\circ$  ( $\epsilon \sim 0.78$ ; Figure 13). This may imply that we have bad phase solutions,

<sup>27</sup> <http://www.alma.cl/~skameno/AMAPOLA/>

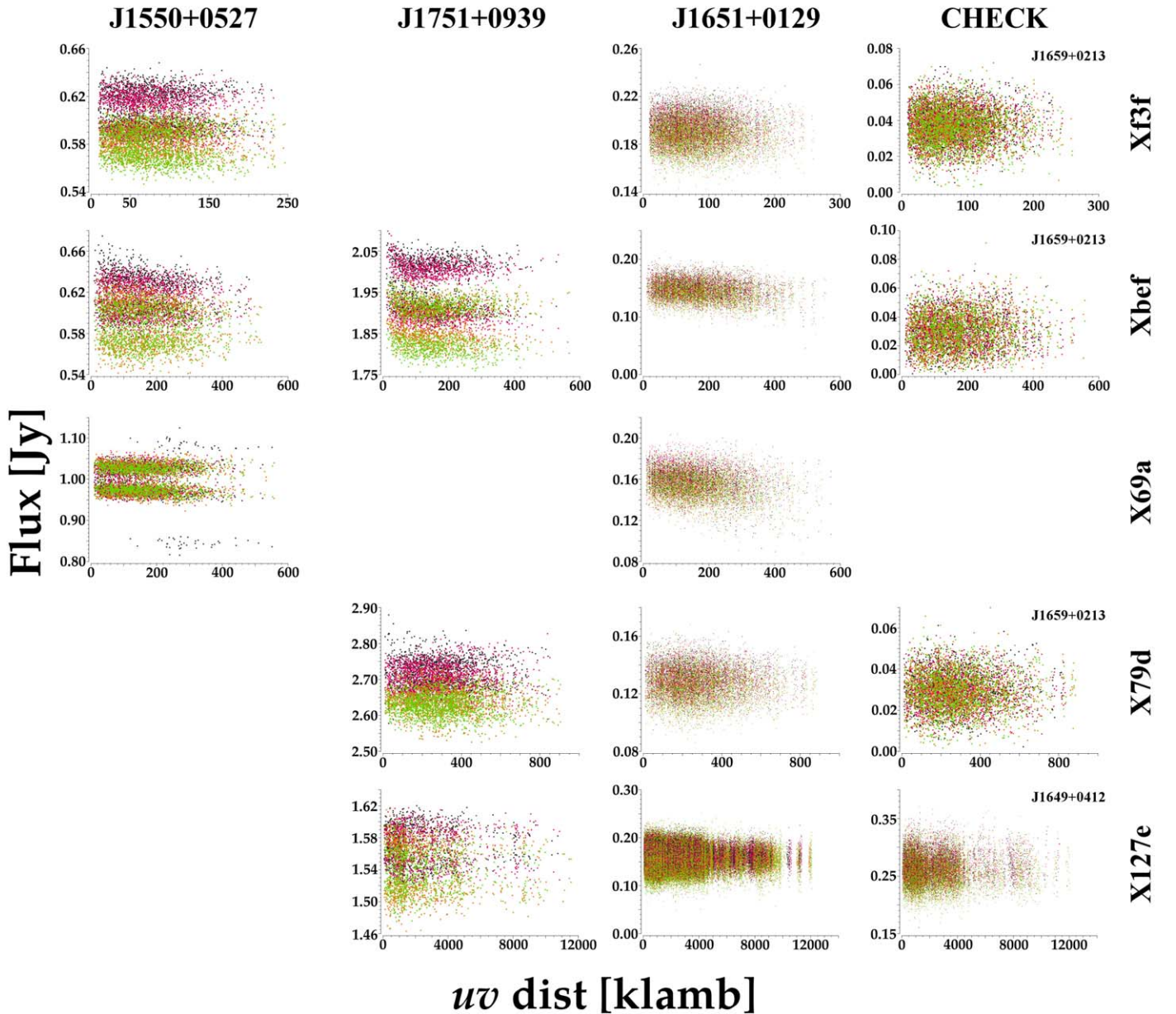


**Figure 12.** Amplitude vs.  $uv$  distance visibility distributions obtained after the WVR solution scaling for the pointlike sources used as calibrators in the observations considered in this work.

in agreement with the large phase spread in Figure 13. To address this, we self-calibrated the check-source data once (a single instance) assuming a pointlike source model at the phase center. The solution interval was set per integration, and no solution was rejected at the  $3\sigma$  level. Table 2 summarizes the results assuming different precalibration strategies. As one can see, depending on whether the peak- or integrated-flux ratios are considered, there is a signal decorrelation of 25%–50% (the smaller value being in agreement with the observed phase scatter of  $\sim 40^\circ$ ). After self-calibration, we measure a flux of  $\sim 260$  mJy for the check source, compared to initial peak and integrated fluxes of 130 and 190 mJy, respectively. This relatively weak phase stability, combined with the sparse  $uv$  coverage for long baselines, particularly affects continuum measurements at scales of  $\sim 1''$ , as presented in Section 3.2, but the  $^{12}\text{CO}(2-1)$  analysis is at a much lower (negligible) level,

since this was done using a much narrower frequency range, based on a feathering process on a per-channel basis.

#### A.1.2. Self-calibrating Xc5148b/X127e

The previous section shows that a significant level of signal decorrelation is affecting the data. This is inducing an overestimate of the total source flux at large scales, since much of the line flux is extended (i.e., integrated to a peak flux ratio  $>1$ ). For this reason, we have adopted a stepwise self-calibration approach in baseline length. We first used the compact and intermediate configuration data sets to image the source. These covered the baseline range of  $<800$  k $\lambda$  (baseline lengths can be converted to km by multiplying by a factor of 0.00133), which partly overlaps with those in Xc5148b/X127e. We thus used the first model image (from nonextended configurations) to self-calibrate only those antennas in

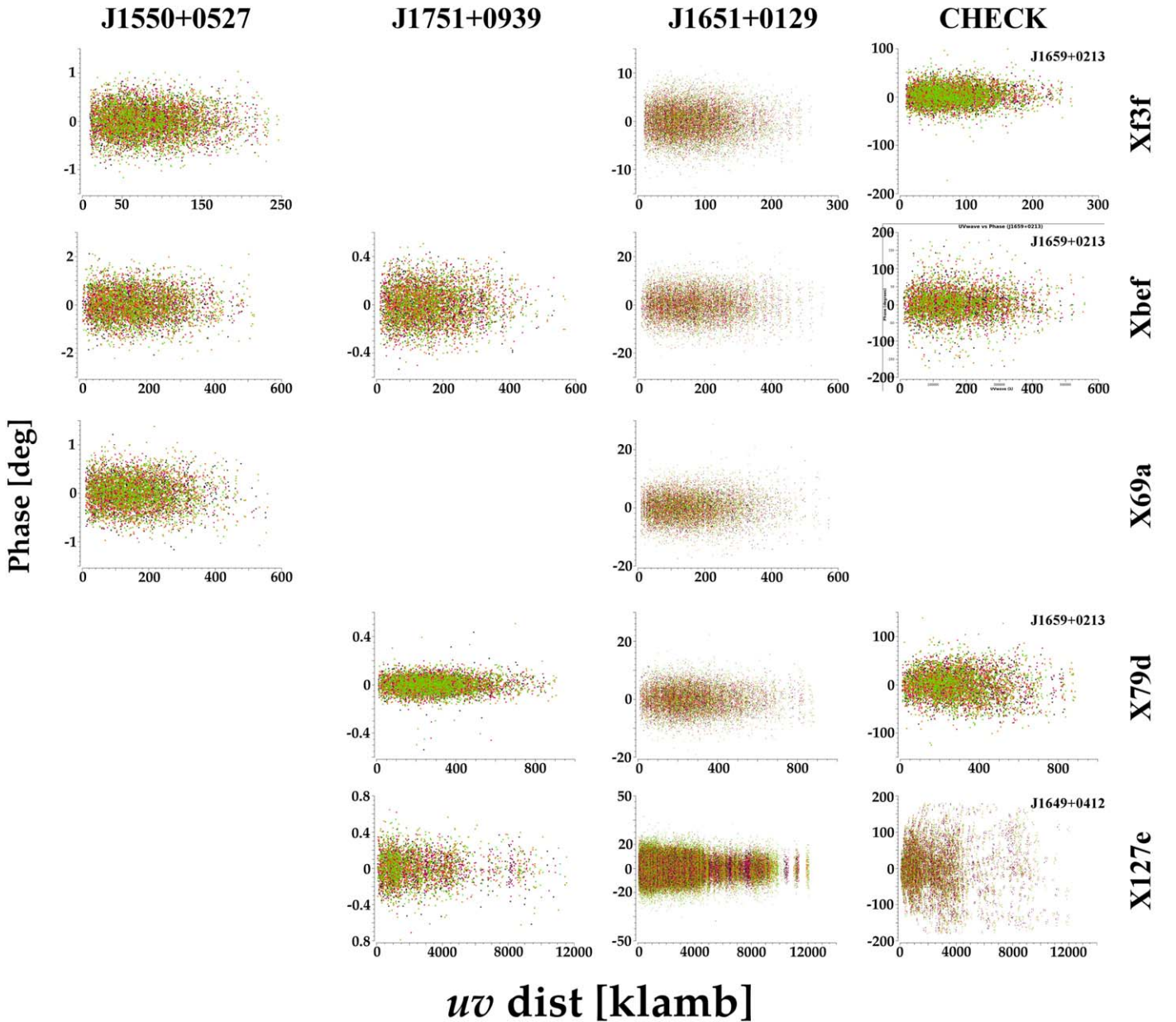


**Figure 13.** Phase vs.  $uv$  distance visibility distributions obtained after the WVR solution scaling for the pointlike sources used as calibrators in the observations considered in this work.

Xc5148b/X127e that have at least three baselines in the overlapping range. Note that these antennas have longer baselines between themselves, which means that after self-calibration, one can retrieve a higher-resolution image making use of those baselines longer than the previous cut (in our case,  $<800$  versus  $<2400$   $k\lambda$ ). This new image allows the calibration of other antennas at longer baselines. Such a stepwise (“unfolding”) approach was considered using the following baseline cuts: 800, 2400, 4000, and 8000  $k\lambda$ . Each self-calibration step only accepted per-antenna solutions when at least three baselines were available within the baseline length cut and the significance was greater than  $1.5\sigma$  (probability greater than 86.6%). The solutions were found per scan and averaged over both polarizations (gaintype = T), since no significant difference between XX and YY phase solutions was found. Each step always achieved less than 10% rejected solutions, with the last phase-calibration step at  $<8000$   $k\lambda$

achieving 9.1% rejection of the data initially available for self-calibration (i.e., after the usual phase-referencing calibration). The final calibration adopted WVR scaling with DA61 flagged and the “unfolding” self-calibration strategy applied.

### A.1.3. Imaging Parameters

Once all of the data reduction and calibration steps described above were performed, we carried out the imaging process in order to create the final data cube. This was done using a natural weighting scheme that led to a beam size on the  $^{12}\text{CO}(2-1)$  line cube of  $0''.06 \times 0''.032$  at an angle of  $-72^\circ$ . While we experimented with several spectral bin sizes, the final cube had a resolution of  $20 \text{ km s}^{-1}$ . The final rms of the cube is  $\sim 0.28 \text{ mJy beam}^{-1}$ . From this cube, we created the moment 0 map described in more detail in Section 3.1 by integrating the line emission between  $-500$  and  $980 \text{ km s}^{-1}$ . The rms of this

**Table 2**  
The Self-calibration (Selfcal) Results on the Check Source for Different Precalibration Strategies

WVRsc [Y/N]	Flagged Antennae	Peak (mJy)	$1 - \epsilon$ (%)	Integ. (mJy)	$1 - \epsilon$ (%)	Integ./Peak	Off (mas)
Y	DA61	132 ± 4 261.9 ± 0.2	50 ± 1	190 ± 10 261.3 ± 0.3	28 ± 2	1.4 ± 0.1 0.998 ± 0.001	14 0
N	DA61	132 ± 5 261.9 ± 0.2	50 ± 1	190 ± 10 261.3 ± 0.3	27 ± 2	1.5 ± 0.1 0.998 ± 0.001	13 0
Y	High phase	167 ± 4 262.1 ± 0.2	36.3 ± 0.6	196 ± 9 262.2 ± 0.4	25 ± 1	1.18 ± 0.06 1.000 ± 0.002	15 0

**Note.** The first and second sets of rows consider water vapor radiometer (WVR) scaling being applied (Y) or not (N), respectively. The third set of rows shows the results when antennas with high phase rms ( $\sigma_\phi > 1$  rad or  $57^\circ$ ) are flagged in addition to DA61 (see text for more details). In each set of rows, the first and second refer to the pre- and post-selfcal observed values, respectively. The decorrelation factors (in %) between the selfcal'ed and not selfcal'ed values are shown in the second row in each set. The last column shows the offset between the source and the phase centers in milliarcseconds.

moment 0 map is  $0.04 \text{ Jy beam}^{-1} \text{ km s}^{-1}$ . For the continuum map discussed in Section 3.2, the resulting beam size is  $0''.078 \times 0''.047$  at an angle of  $-73^\circ$ , while the rms of the final image is  $0.024 \text{ mJy beam}^{-1}$ . From the  $^{12}\text{CO}(2-1)$  line cube, we also created moment 1 (velocity) and moment 2 (velocity dispersion) maps. The *immoments* CASA task was used for this purpose. A  $3\sigma$  threshold on the total flux was used to create the moment 1 map, while a  $5\sigma$  limit was considered for the velocity dispersion image. These choices are mostly aesthetic and do not have a significant impact on our analysis.

### ORCID iDs

Ezequiel Treister  <https://orcid.org/0000-0001-7568-6412>  
Hugo Messias  <https://orcid.org/0000-0002-2985-7994>  
George C. Privon  <https://orcid.org/0000-0003-3474-1125>  
Neil Nagar  <https://orcid.org/0000-0001-6920-662X>  
Anne M. Medling  <https://orcid.org/0000-0001-7421-2944>  
Vivian U  <https://orcid.org/0000-0002-1912-0024>  
Franz E. Bauer  <https://orcid.org/0000-0002-8686-8737>  
Claudia Cicone  <https://orcid.org/0000-0003-0522-6941>  
Loreto Barcos Muñoz  <https://orcid.org/0000-0003-0057-8892>  
Aaron S. Evans  <https://orcid.org/0000-0003-2638-1334>  
Francisco Muller-Sanchez  <https://orcid.org/0000-0002-2713-0628>  
Julia M. Comerford  <https://orcid.org/0000-0001-8627-4907>  
Lee Armus  <https://orcid.org/0000-0003-3498-2973>  
Chin-Shin Chang  <https://orcid.org/0000-0001-9910-3234>  
Michael Koss  <https://orcid.org/0000-0002-7998-9581>  
Giacomo Venturi  <https://orcid.org/0000-0001-8349-3055>  
Kevin Schawinski  <https://orcid.org/0000-0001-5464-0888>  
Caitlin Casey  <https://orcid.org/0000-0002-0930-6466>  
C. Megan Urry  <https://orcid.org/0000-0002-0745-9792>  
David B. Sanders  <https://orcid.org/0000-0002-1233-9998>  
Nicholas Scoville  <https://orcid.org/0000-0002-0438-3323>  
Kartik Sheth  <https://orcid.org/0000-0002-5496-4118>

### References

- Baan, W. A., Hagiwara, Y., & Hofner, P. 2007, *ApJ*, 661, 173  
Barnes, J. E., & Hernquist, L. E. 1991, *ApJL*, 370, L65  
Baumgartner, W. H., Tueller, J., Markwardt, C. B., et al. 2013, *ApJS*, 207, 19  
Beswick, R. J., Pedlar, A., Mundell, C. G., & Gallimore, J. F. 2001, *MNRAS*, 325, 151  
Blecha, L., Loeb, A., & Narayan, R. 2013, *MNRAS*, 429, 2594  
Blecha, L., Snyder, G. F., Satyapal, S., & Ellison, S. L. 2018, *MNRAS*, 478, 3056  
Bolatto, A. D., Wolfire, M., & Leroy, A. K. 2013, *ARA&A*, 51, 207  
Bournaud, F., Chapon, D., Teyssier, R., et al. 2011, *ApJ*, 730, 4  
Bryant, P. M., & Scoville, N. Z. 1999, *AJ*, 117, 2632  
Cicone, C., Severgnini, P., Papadopoulos, P. P., et al. 2018, *ApJ*, 863, 143  
Dale, D. A., Sheth, K., Helou, G., et al. 2005, *AJ*, 129, 2197  
de Vaucouleurs, G. H., de Vaucouleurs, A., & Shapley, H. 1964, Reference Catalog of Bright Galaxies (Austin, TX: Univ. Texas Press)  
Donley, J. L., Kartaltepe, J., Kocevski, D., et al. 2018, *ApJ*, 853, 63  
Downes, D., & Solomon, P. M. 1998, *ApJ*, 507, 615  
Engel, H., Davies, R. I., Genzel, R., et al. 2010, *A&A*, 524, A56  
Fan, L., Han, Y., Fang, G., et al. 2016, *ApJL*, 822, L32  
Feruglio, C., Fiore, F., Maiolino, R., et al. 2013a, *A&A*, 549, A51  
Feruglio, C., Fiore, F., Piconcelli, E., et al. 2013b, *A&A*, 558, A87  
Gerssen, J., van der Marel, R. P., Axon, D., et al. 2004, *AJ*, 127, 75  
Glikman, E., Simmons, B., Mailly, M., et al. 2015, *ApJ*, 806, 218  
Goulding, A. D., Greene, J. E., Bezanson, R., et al. 2018, *PASJ*, 70, S37  
Greve, T. R., Papadopoulos, P. P., Gao, Y., et al. 2009, *ApJ*, 692, 1432  
Hagiwara, Y., Baan, W. A., & Klöckner, H.-R. 2011, *AJ*, 142, 17  
Heckman, T. M., Armus, L., & Miley, G. K. 1990, *ApJS*, 74, 833  
Herrero-Illana, R., Privon, G. C., Evans, A. S., et al. 2019, *A&A*, 628, A71  
Hinshaw, G., Weiland, J. L., Hill, R. S., et al. 2009, *ApJS*, 180, 225  
Hopkins, P. F., Hernquist, L., Cox, T. J., & Kereš, D. 2008, *ApJS*, 175, 356  
Howell, J. H., Armus, L., Mazzarella, J. M., et al. 2010, *ApJ*, 715, 572  
Inami, H., Armus, L., Charmandaris, V., et al. 2013, *ApJ*, 777, 156  
Iono, D., Wilson, C. D., Takakuwa, S., et al. 2007, *ApJ*, 659, 283  
Kocevski, D. D., Brightman, M., Nandra, K., et al. 2015, *ApJ*, 814, 104  
Kollatschny, W., Weilbacher, P. M., Ochmann, M. W., et al. 2020, *A&A*, 633, A79  
Komossa, S., Burwitz, V., Hasinger, G., et al. 2003, *ApJL*, 582, L15  
Lutz, D., Sturm, E., Janssen, A., et al. 2020, *A&A*, 633, A134  
Maiolino, R., Gallerani, S., Neri, R., et al. 2012, *MNRAS*, 425, L66  
Maud, L. T., Tilanus, R. P. J., van Kempen, T. A., et al. 2017, *A&A*, 605, A121  
Max, C. E., Canalizo, G., & de Vries, W. H. 2007, *Sci*, 316, 1877  
Max, C. E., Canalizo, G., Macintosh, B. A., et al. 2005, *ApJ*, 621, 738  
McMullin, J. P., Waters, B., Schiebel, D., Young, W., & Golap, K. 2007, in ASP Conf. Ser. 376, Astronomical Data Analysis Software and Systems XVI, ed. R. A. Shaw, F. Hill, & D. J. Bell (San Francisco, CA: ASP), 127  
Medling, A. M., Ammons, S. M., Max, C. E., et al. 2011, *ApJ*, 743, 32  
Medling, A. M., Privon, G. C., Barcos-Muñoz, L., et al. 2019, *ApJL*, 885, L21  
Medling, A. M., U, V., Guedes, J., et al. 2014, *ApJ*, 784, 70  
Medling, A. M., U, V., Guedes, J., et al. 2015, *ApJ*, 803, 61  
Meijerink, R., Kristensen, L. E., Weiß, A., et al. 2013, *ApJL*, 762, L16  
Moster, B. P., Somerville, R. S., Maulbetsch, C., et al. 2010, *ApJ*, 710, 903  
Müller Sánchez, F., Davies, R. I., Eisenhauer, F., et al. 2006, *A&A*, 454, 481  
Müller-Sánchez, F., Nevin, R., Comerford, J. M., et al. 2018, *Natur*, 556, 345  
Murray, N. 2011, *ApJ*, 729, 133  
Nakanishi, K., Okumura, S. K., Kohno, K., et al. 2005, *PASJ*, 57, 575  
Nandra, K., & Pounds, K. A. 1994, *MNRAS*, 268, 405  
Nardini, E., Wang, J., Fabbiano, G., et al. 2013, *ApJ*, 765, 141  
Ochsendorf, B. B., Meixner, M., Roman-Duval, J., Rahman, M., & Evans, N. J., II 2017, *ApJ*, 841, 109

- Papadopoulos, P. P., van der Werf, P., Xilouris, E., Isaak, K. G., & Gao, Y. 2012, *ApJ*, 751, 10
- Papadopoulos, P. P., Zhang, Z.-Y., Xilouris, E. M., et al. 2014, *ApJ*, 788, 153
- Pasquali, A., Gallagher, J. S., & de Grijs, R. 2004, *A&A*, 415, 103
- Planck Collaboration, Ade, P. A. R., Aghanim, N., et al. 2011, *A&A*, 536, A19
- Saito, T., Iono, D., Ueda, J., et al. 2018, *MNRAS*, 475, L52
- Sanders, D. B., Soifer, B. T., Elias, J. H., et al. 1988, *ApJ*, 325, 74
- Scoville, N., Aussel, H., Sheth, K., et al. 2014, *ApJ*, 783, 84
- Scoville, N., Sheth, K., Aussel, H., et al. 2016, *ApJ*, 820, 83
- Scoville, N., Sheth, K., Walter, F., et al. 2015, *ApJ*, 800, 70
- Scoville, N. Z., Evans, A. S., Thompson, R., et al. 2000, *AJ*, 119, 991
- Solomon, P. M., Downes, D., Radford, S. J. E., & Barrett, J. W. 1997, *ApJ*, 478, 144
- Solomon, P. M., & Vanden Bout, P. A. 2005, *ARA&A*, 43, 677
- Stierwalt, S., Armus, L., Surace, J. A., et al. 2013, *ApJS*, 206, 1
- Tacconi, L. J., Genzel, R., Smail, I., et al. 2008, *ApJ*, 680, 246
- Tacconi, L. J., Genzel, R., Tecza, M., et al. 1999, *ApJ*, 524, 732
- Tecza, M., Genzel, R., Tacconi, L. J., et al. 2000, *ApJ*, 537, 178
- Trakhtenbrot, B., Lira, P., Netzer, H., et al. 2017, *ApJ*, 836, 8
- Treister, E., Privon, G. C., Sartori, L. F., et al. 2018, *ApJ*, 854, 83
- Treister, E., Schawinski, K., Urry, C. M., & Simmons, B. D. 2012, *ApJL*, 758, L39
- Tunnard, R., Greve, T. R., Garcia-Burillo, S., et al. 2015, *ApJ*, 815, 114
- U, V., Wang, Z., Sanders, D., et al. 2011, in ASP Conf. Ser. 446, *Galaxy Evolution: Infrared to Millimeter Wavelength Perspective*, ed. W. Wang et al. (San Francisco, CA: ASP), 97
- Van Wassenhove, S., Volonteri, M., Mayer, L., et al. 2012, *ApJL*, 748, L7
- Veilleux, S., et al. 2009, *ApJS*, 182, 628
- Wang, J., Nardini, E., Fabbiano, G., et al. 2014, *ApJ*, 781, 55
- Weigel, A. K., Schawinski, K., Treister, E., Trakhtenbrot, B., & Sanders, D. B. 2018, *MNRAS*, 476, 2308
- Weston, M. E., McIntosh, D. H., Brodwin, M., et al. 2017, *MNRAS*, 464, 3882
- Wilson, C. D., Petitpas, G. R., Iono, D., et al. 2008, *ApJS*, 178, 189
- Yamashita, T., Komugi, S., Matsuhara, H., et al. 2017, *ApJ*, 844, 96